# A global map of meso-scale eddy diffusivities based on linear stability analysis

**Master Thesis in Physical Oceanography**

**presented to the Department of Geosciences**

**University of Hamburg**

**supervised by Prof. Dr. Carsten Eden**

Lukas Vollmer

January 4, 2013

# Contents

# 1. Introduction

Processes in the ocean occur on a variety of time- and lengthscales. The exchange between the deep and the upper ocean is a process, that can take several hundred years. Dominant currents in the different global ocean basins have decadal and seasonal variations. On a smaller lengthscale an eddy circulation occurs on timescales of days to weeks, and on the smallest lengthscale of millimeters, momentum is dissipated in instants of a second. One of the central questions in modern physical oceanography is how the different scales interact with each other and how they combine to transport heat and material from the equator towards the poles.

The evolution of computer resources allows to implement ocean models on increasing high resolution. A sufficient high resolution enables to resolve the eddy structure of the so-called meso-scale ocean circulation and allows to study the effect of eddies on the large-scale circulation. Low resolution models rely on the knowledge about eddy contribution to the mean flow. These models are supposed to run for decades to predict future climate changes and test climate sensivity. As low resolution models are not able to resolve meso-scale features, these features have to be parametrized.

Two different popular approaches exist to an parametrization of meso-scale effects. An approach by *Marshall* (1981) and an approach by *Gent and McWilliams* (1990) . *Marshall* (1981) propose a parametrization of meso-scale mixing of quasi-geostrophic potential vorticity fluxes. The parametrization is implemented in the mean momentum equation. The advantage of this method is that potential vorticity (PV) is solely capable of representing the structure of the large scale circulation. Furthermore *Eden* (2010) shows that a parametrization based on PV is able to reproduce the observed phenomena

of zonal jets. Zonal jets are driven by interaction between the large- and the meso-scale. Most ocean models are based on an alternative approach, that implements a parametrization in the mean density budget.

First proposed by *Gent and McWilliams* (1990), the parametrization focuses on meso-scale density fluxes. *Gent and McWilliams* (1990) consider the effect of meso-scale eddies on the mean density field. Eddies are created by a release of large-scale energy. They reduce the mean available potential energy of the ocean, that is stored in the sloping isopycnals created by global wind-curls and heat fluxes.

Both *Marshall* (1981) and *Gent and McWilliams* (1990) relate the meso-scale fluxes of the regarded variable to the mean gradient of the variable. The parametrization by Gent and McWilliams is given by a diffusivity $\kappa_b$ multiplied by the isopycnal slope vector. Hence a release of energy by eddies proportionally to the strength of the density gradient will occur, where horizontal density gradients exist. The diffusivity $\kappa_b$ is also called thickness diffusivity, because it was derived from a model based on isopycnal coordinates. Thickness diffusivity does not describe a diffusive mixing of density but a redistribution of the thickness of isopycnal layers. Likewise the parametrization by Marshall is given by a diffusivity $\kappa_{pv}$ multiplied by the mean PV gradient. In this procedure PV is redistributed along its mean gradient.

As it is not well understood which processes influence the magnitudes of the different eddy diffusivities, their values were kept constant in first models using the parametrizations.

Significant horizontal variations in eddy diffusivity were suggested from surface altimetry by *Stammer* (1998), *Bauer et al.* (2002) and *Marshall et al.* (2006). Recently, vertical distributions for eddy diffusivities are obtained from high resolution models. Various studies (e.g. *Eden* (2006), *Eden et al.* (2007), *Abernathey et al.* (2010)) reveal that the diffusivity varies in several orders of magnitude, with maximum values located in the vicinity of strong currents.

*Eden et al.* (2009) show that a varying $\kappa_b$ has systematic influences on the mean hydrographic properties by comparing different closures for the thickness diffusivity $\kappa_b$ in a

coarse global ocean model. They observe amongst other a dependence of the equatorial thermocline depth and the pathway of the Gulf Stream extension on different distributions of $\kappa_b$. The three approaches compared in the study each rely on one or more ocean properties. These properties are the local stratification, the vertical shear of velocities, and an eddy length scale. The size of the eddy length scale and the vertical structure of thickness diffusivity are chosen to be close to estimates from observations or models. The spatial dependency of thickness diffusivity is lacking a profound physical explanation.

A physically meaningful spatial dependency of the diffusivities $\kappa_b$ and $\kappa_{pv}$ can be obtained from the mean variables of the coarse models through baroclinic linear stability analysis (LSA) (*Green* (1970)).

Meso-scale turbulence is generated by an unstable mean flow, that is resolved in the model. In a linear approximation the unstable mean flow is favoring the growth of a certain bandwidth of waves, that tend to grow to turbulent eddies. The full instability problem is quite complex, thus most studies make use of a local approximation. Using this approximation *Gill et al.* (1974) and *Robinson and McWilliams* (1974) show that ocean currents are baroclinically unstable on scales consistent with observations. The local approximation assumes, that the properties of the mean flow at a certain location are constant at the scale of the excited wave. This approximation is valid for most regions of the ocean, where barotropic instability created by the horizontal velocity shear is negligible and where topographic slopes are flat.

The local approximation does not provide all of the dynamics, that play a role in eddy formation, including the radiation of instabilities from boundary currents into the interior (*Hristova et al.* (2010)) and the eddy feedback on the mean flow. However, the local assumption provides a well-defined prediction and is the starting point for most meso-scale ocean eddy theories.

*Killworth* (1997) explored a closure of eddy diffusivities $\kappa$ based on linear stability theory following a suggestion of *Green* (1970). The closure used in the following is proposed in *Eden* (2011) and based on the idea of Killworth. The advantage of the closure is

a spatial distribution, that is a direct consequence of linear stability analysis without further assumptions. Furthermore the closure can consider factors like depth-dependent shear and stratification. Linear stability analysis also allows to study stabilization or destabilization by a lateral dependent Coriolis force or by topography.
None of these factors are component of present closures.
In this study we use linear stability analysis on constructed exemplary ocean background conditions to understand the spatial dependency of meso-scale eddy diffusivities. We make use of the advantages of LSA to study the influences of depth-dependent shear and stratification as well as topography and a lateral dependent Coriolis force. The knowledge gained from the exemplary conditions is used to explain the spatial dependency of eddy diffusivities, that are calculated by LSA for a global climatology, that is based on observations (WOCE by *Gouretski and Koltermann* (2004)).
The goal is to understand, which oceanic background conditions lead to different vertical and horizontal structures of diffusivities originating from baroclinic instability. The detailed structure of the thesis is as following.
In the first part, parametrizations for buoyancy and momentum fluxes are derived and the closure based on linear stability theory is presented.
The results consist of four sections. The first is dealing with simple constructed profiles to illustrate how LSA works and which vertical distributions of eddy diffusivities it produces. The dependency of the solution on depth-dependent velocity shear, planetary vorticity, and topography is studied using these profiles. In the second section example profiles of the climatology are analyzed. The third section deals with the global distribution of eddy growthrates and eddy lengthscales and in the fourth section we show global maps and transects of diffusivities, that result from the closure. We compare the results to an approximate solution, that is not able to represent all effects included in LSA.
In the discussion limits of the closure are pointed out and the eddy diffusivities are compared to results from observational and model studies.

# 2. Methods

## 2.1. Parametrization of meso-scale fluxes

To derive a parametrization for meso-scale fluxes we start with the primitive equations in Boussinesq and hydrostatic approximation. Neglecting any friction or source terms, they can be written as

$$\frac{\partial \mathbf{u}_h}{\partial t} + \mathbf{u}_h \cdot \nabla_h \mathbf{u}_h + f \underset{\neg}{\mathbf{u}_h} = -\nabla_h p \tag{2.1}$$

$$b = \frac{\partial p}{\partial z} \tag{2.2}$$

$$\frac{\partial b}{\partial t} + \mathbf{u}_h \cdot \nabla_h b + w N^2 = 0 \tag{2.3}$$

$$\nabla \mathbf{u} = 0 \tag{2.4}$$

The two horizontal momentum equations are combined to one term in eq. (2.1) in which the vertical advection of momentum is assumed to be small and is neglected. The horizontal velocities and derivatives are expressed as $\mathbf{u}_h = (u, v)$ and $\nabla_h = (\partial/\partial x, \partial/\partial y)$. The pressure p denotes pressure divided by the reference density $\rho_0$, f is the inertial frequency. Vectors with the subscript $\underset{\neg}{..}$ are rotated by 90° in the horizontal plane, i.e. $\underset{\neg}{\mathbf{u}_h} = (-v, u)$. Equation (2.2) is the hydrostatic relation, introducing buoyancy $b = -g\rho/\rho_0$. In the buoyancy budget (2.3), the advection of buoyancy is divided into a horizontal and a vertical part. This is an allowed simplification, when horizontal

buoyancy gradients are small compared to the vertical gradient and when the vertical velocity $w$ is small compared to horizontal velocities. The vertical buoyancy gradient is expressed here by the Brunt–Väisälä frequency $N = \sqrt{\frac{\partial b}{\partial z}}$. These conditions are valid almost everywhere in the ocean with exception of the surface mixed layer. The last equation (2.4) is the continuity equation in an incompressible fluid.

To separate the slowly varying circulation from the short-term circulation, the variables are divided into a mean part and a perturbation part $x = \overline{x} + x'$. The perturbation part vanishes, when applying the temporal mean operator $\overline{x'} = 0$. When applying the operator on a product of two or more perturbation variables, the result represents a correlation term, which usually does not vanish, e.g. $\overline{x'x'} \neq 0$ or $\overline{x'y'} \neq 0$. Applying on the momentum and the buoyancy equation yields

$$\frac{\partial \overline{\mathbf{u}_h}}{\partial t} + \overline{\mathbf{u}_h} \cdot \nabla_h \overline{\mathbf{u}_h} + f \overline{\mathbf{u}_\mathbf{h}}_{\neg} + \nabla_h \overline{p} = -\overline{\mathbf{u'}_h \cdot \nabla_h \mathbf{u'}_h} \tag{2.5}$$

$$\frac{\partial \overline{b}}{\partial t} + \overline{\mathbf{u}}_h \cdot \nabla_h \overline{b} + \overline{w} N^2 = -\overline{\mathbf{u}'_h \nabla_h \cdot b'} \tag{2.6}$$

On the right-hand-side of the equations, the correlation terms show up, which need to be parametrized if they can not be resolved by the model.

Using the identity $\overline{\mathbf{u}'_h \cdot \nabla_h \mathbf{u}'_h} = \nabla_h \cdot \overline{\mathbf{u}'_h \mathbf{u}'_h}$, the terms can be written as a divergence of a flux term. The term $\overline{\mathbf{u}'_h \mathbf{u}'_h}$, showing up in the momentum equation (2.5), is the eddy momentum flux. The term $\overline{\mathbf{u}'_h b'}$, from the buoyancy equation (2.6), is the eddy buoyancy flux.

## 2.2. Isopycnal mixing

Mixing of material properties by eddies in a stably stratified fluid occurs mainly along isopycnals. Vertical density gradients are usually much larger in the ocean than horizontal gradients with exception of the oceanic mixed layer. Thus isopycnals are usually horizontal. *Gent and McWilliams* (1990) propose a decomposition of eddy fluxes along the horizontal gradients. Following *Killworth* (1997) and *Eden* (2011) the horizontal buoyancy flux in the buoyancy budget can be decomposed as

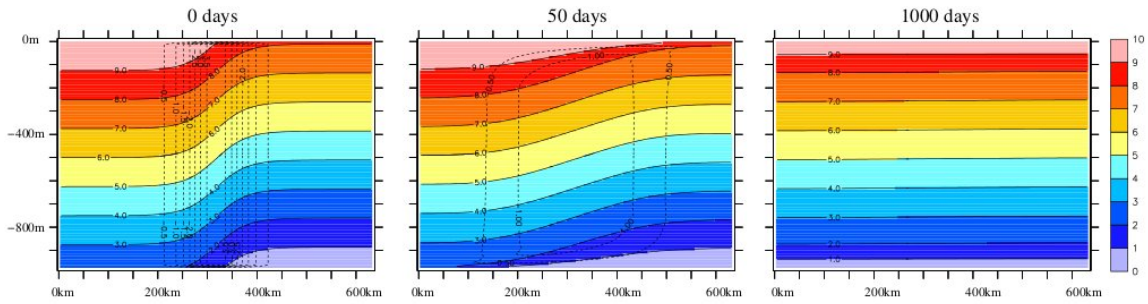


Figure 2.1.: The effect of the parametrization by Gent and McWilliams in an idealized model. Shown are mean isothermes in $°C$ (in this case proportional to the mean buoyancy $\overline{b}$) in colors and the contour lines of the streamfunction of the eddy-driven velocity for three subsequent times (from *Olbers et al.* (2012))

$$\overline{\mathbf{u}_h' b'} = -\kappa_b \nabla_h \overline{b} + \nu_b \underline{\nabla \overline{b}} \tag{2.7}$$

The first term on the right-hand-side of equation (2.7) is a downgradient term related to the removal or production of mean available potential energy by the eddy induced circulation. A positive $\kappa_b$ would cause a release of mean available potential energy. If $\kappa_b = 0$, the eddy induced circulation has no effect on the mean circulation. The second term represents a skewness diffusivity along the isopycnals. The physical meaning of $\nu_b$ is, that it is a streamfunction for eddy advection of mean isopycnal thickness (*Eden et al.* (2007)). It is not included in the initial parametrization by Gent and McWilliams and has no influence on the balance of potential energy, but it becomes important regarding passive tracers. The flux term in equation (2.6) can be interpreted as a mean vertical eddy-driven advection velocity term $w^e = \nabla_h \overline{\mathbf{u}_h' b'}/N^2$, which can be added to the background velocity to form the residual vertical velocity $w^* = \overline{w} + w^e$. Replacing the flux term in the buoyancy budget, equation (2.6) becomes

$$\frac{\partial \overline{b}}{\partial t} + \overline{\mathbf{u}}_h \cdot \nabla_h \overline{b} + (\overline{w} + w^e) N^2 = 0 \tag{2.8}$$

with

$$w_e = \frac{\nabla_h \overline{\mathbf{u}_h' b'}}{N^2} = \nabla_h \left( -\frac{\kappa_b \nabla_h \bar{b}}{N^2} + \frac{\nu_b \underline{\nabla} \bar{b}}{N^2} \right) = \nabla_h (-\kappa_b \mathbf{s} + \nu_b \underline{\mathbf{s}}) \tag{2.9}$$

, in which $\mathbf{s} = -\nabla_h \bar{b}/N^2$ is the isopycnal slope vector. The horizontal eddy buoyancy flux essentially produces a vertical advection of background buoyancy. Diapycnal diffusion of buoyancy does not occur, so the volume of isopycnals does not change over the whole domain. This effect is also called thickness diffusion, because the vertical thickness of the isopycnals is redistributed in the process (see fig.2.1). A dominant downgradient flux, as expected in most domains, leads to a flattening of isopycnal slopes and therefor a decrease of available potential energy.
Using the continuity equation $\partial w^e/\partial z + \nabla \mathbf{u}_h^e = 0$ on the eddy-driven velocity, we receive its horizontal part.

$$\mathbf{u}_h^e = -\partial/\partial z \frac{\overline{\mathbf{u}_h' b'}}{N^2} = \partial/\partial z (\kappa_b \mathbf{s} - \nu_b \underline{\mathbf{s}}) \tag{2.10}$$

## 2.3. Mixing in the momentum equation

The parametrization of the flux term $\overline{\mathbf{u}_h' \mathbf{u}_h'}$ in the momentum equation (2.5) analogous to the parametrization in chapter 2.2 fails, since eddy momentum fluxes do not have a clear relation to the mean momentum gradient. One flux, that is expected to be related to its mean gradient, is the eddy potential vorticity (PV) flux. The quasi-geostrophic potential vorticity is given by

$$q = \beta y + \underline{\nabla} \cdot \mathbf{u}_h + \frac{\partial}{\partial z} \left( \frac{f}{N^2} b \right) \tag{2.11}$$

The terms represent planetary vorticity, relative vorticity and a stretching vorticity term, respectively. From equation (2.11) an eddy PV flux can be derived.

$$\overline{\underline{\mathbf{u}_h}' q'} = \nabla \cdot \overline{\mathbf{u}_h' \mathbf{u}_h'} - f \underline{\mathbf{u}_h}^e + \nabla_h \left( \frac{\overline{b'^2}}{2N^2} - \frac{\overline{|\mathbf{u}_h'|^2}}{2} \right) \tag{2.12}$$

This flux is already rotated by 90° (see *Olbers et al.* (2012) p.392 for the derivation of this term). Using (2.12) to replace the divergence of eddy momentum flux, the momentum equation can be written as

$$\frac{\partial \overline{\mathbf{u}_h}}{\partial t} + \overline{\mathbf{u}_h} \cdot \nabla_h \overline{\mathbf{u}_h} + f \overline{\mathbf{u}_h}^* = -\nabla_h \overline{p} + \nabla_h \left( \frac{\overline{b'^2}}{2N^2} - \frac{\overline{|\mathbf{u}_h'|^2}}{2} \right) - \overline{\mathbf{u}'}_h \, q' \tag{2.13}$$

Like the eddy buoyancy flux, the eddy PV flux can be composed into a horizontal downgradient term and a term along constant vorticity.

$$\overline{\mathbf{u}' q'} = -\kappa_{pv} \nabla_h \overline{q} + \nu_{pv} \underset{\neg}{\nabla} \overline{q} + \underset{\neg}{\nabla} \Theta \tag{2.14}$$

The term $\Theta = \nabla_h \left( \frac{\overline{b'^2}}{2N^2} - \frac{\overline{|\mathbf{u}_h'|^2}}{2} \right)$ in (2.14) originates from the eddy vorticity flux equation and therefor has to be included in the parametrization of $\overline{\mathbf{u}' q'}$. Using (2.14) in the momentum equation provides the equations, that include both parametrizations

$$\frac{d \overline{\mathbf{u}_h}^*}{dt} + f \overline{\mathbf{u}_h}^* = -\nabla_h \overline{p} + \kappa_{pv} \underset{\neg}{\nabla} \overline{q} + \nu_{pv} \nabla_h \overline{q} + \nabla_h \Theta \tag{2.15}$$

$$\frac{\partial \overline{b}}{\partial t} + \overline{\mathbf{u}}_h \cdot \nabla_h \overline{b} + \overline{w}^* N^2 = 0 \tag{2.16}$$

These two equations represent the different approaches of implementing the effect of the meso-scale circulation in a mean model. The first one is the implementation in the mean momentum equation by parametrizing eddy PV fluxes following *Marshall* (1981) and the second one is the implementation by parametrizing eddy buoyancy fluxes in the mean buoyancy equation following *Gent and McWilliams* (1990). The only variables, that still need to be obtained to close the parametrizations are either $\kappa_{pv}$ and $\nu_{pv}$ or $\kappa_b$ and $\nu_b$.

## 2.4. Linear stability analysis

Meso-scale eddy fluxes can be obtained from the linear wave solution $\psi'$ of the perturbed quasi-geostrophic flow (*Killworth* (1997), *Eden* (2011)). Quasi-geostrophy is a further

simplification of the governing equations (2.1 - 2.4), by supposing vanishing mean vertical velocity and vanishing mean horizontal momentum advection. The second assumption relies heavily on the relation between the term $f\overline{\mathbf{u}}_{\mathbf{h}}^{\neg}$ in the mean momentum equation (2.5), that describes the balance of the flow by the Coriolis-force and the term $\overline{\mathbf{u}_h} \cdot \nabla_h \overline{\mathbf{u}_h}$, that describes horizontal advection. Only if the first term dominates, the mean flow is in geostrophic balance and can be described by a quasi-geostrophic streamfunction $\psi$. Thus at the equator, where $f \to 0$, quasi-geostrophy is not applicable. The quasi-geostrophic streamfunction $\psi = \Psi + \psi'$ is decomposed into a steady basic state $\Psi$ and a perturbation $\psi'$. The properties of the flow, that can be derived from the streamfunction, are the mean horizontal velocities $\overline{\mathbf{u}_h} = \underset{\neg}{\nabla}\Psi$, the mean buoyancy $\bar{b} = f\partial_z\Psi$ and the mean potential vorticity $\bar{q} = \nabla^2\Psi + \Gamma\Psi + \beta y$. Introduced here is the vertical operator $\Gamma() = \partial_z(f^2N^{-2}\partial_z())$ for the stretching term in the vorticity equation. The properties of the perturbed flow can be derived in the same way: $\mathbf{u}'_h = \underset{\neg}{\nabla}\psi'$, $b' = f\partial_z\psi'$ and $q' = \nabla^2\psi' + \Gamma\psi'$. In absence of friction quasi-geostrophic potential vorticity is a conserved quantity. Linearized around a basic state that satisfies $\overline{\mathbf{u}_h} \cdot \nabla\overline{q} = 0$ and ignoring terms of second order we obtain

$$\partial_t q' + \overline{\mathbf{u}_h} \cdot \nabla q' + \mathbf{u}'_h \cdot \nabla\overline{q} = 0 \tag{2.17}$$

Considering a flat surface (rigid lid) at z = 0 and a flat bottom at z = -h, the boundary conditions are

$$(\partial_t + \overline{\mathbf{u}_h} \cdot \nabla)\partial_z\psi' = \partial_z\overline{\mathbf{u}_h} \cdot \nabla\psi' \; at \; z = 0, -h \tag{2.18}$$

If we account for bottom slopes and internal friction the equations are slightly modified (see Appendix). Using the local approximation, solutions of equation (2.17) are waves $\psi' = \psi_0\phi(z)e^{-i(\omega t - k_x x - k_y y)}$ on a horizontal plane with a vertical amplitude function $\phi(z)$ that has to satisfy

$$\Gamma\phi = \left(k^2 + \frac{\tilde{\beta}}{c - \tilde{U}}\right)\phi \tag{2.19}$$

in the interior and

$$(\tilde{U} - c)\frac{d\phi}{dz} = \phi\frac{d\tilde{U}}{dz} \; at \; z = 0, -h \tag{2.20}$$

at the boundaries. The phase velocity is given by $c = \omega/k$, with $k = |\mathbf{k}|$ and $\tilde{U} = \mathbf{n} \cdot \overline{\mathbf{u}_h}$, $\tilde{\beta} = -\mathbf{n} \cdot \overline{\nabla} \overline{q}$. The later are the projection of the background velocity respectively vorticity curl in direction of the wave propagation $\mathbf{n} = \mathbf{k}/k$. The boundary conditions correspond to vanishing vertical perturbation velocities at the boundaries. This eigenvalue problem can be discretized in the vertical and be solved numerically. The numeric solution is analogous to the one from *Smith* (2007) and can be found in the Appendix. The eigenfunctions $\phi(z)$ and eigenvalues $\omega$ of the solution might both be complex. For $\mathrm{Im}(\omega) > 0$, the wave amplitude grows exponentially in time. These waves are regarded to dominate the observed wave field. Growing waves can be found for many combinations of $k_x$ and $k_y$. Multiple local maxima in wavenumber-space can be related to different structural vertical modes (*Beckmann* (1988), *Tulloch et al.* (2011)).

## 2.5. A closure for eddy diffusivities

The fastest growing wave can be determined for each vertical oceanic profile. It is characterized by its growth rate $\omega_i = \mathrm{Im}(\omega)$, its phase speed c, its pair of horizontal wavenumbers $k_x$, $k_y$ and its vertical structure $\phi$. The eigenmode $\phi$ is complex attributing a non-dimensional wave amplitude and a phase shift to every depth level of the profile. Properties of the flow can be derived from the perturbation streamfunction $\psi'$ in the same manner as from the geostrophic stream function $\Psi$. The eddy buoyancy flux can be calculated as a cross-correlation of the perturbation velocity and the perturbation buoyancy.

$$\overline{\mathbf{u}_h' b'} = \overline{\overline{\nabla} \psi' \cdot f \partial_z \psi'} = -\frac{\psi_0^2}{2} \mathbf{k} \overline{f} \mathrm{Re}(i \phi \partial_z \phi^*) \tag{2.21}$$

The overbars denote an average over a wave cycle, $\phi^*$ is the complex conjugated eigenfunction. We can define an isotropic buoyancy diffusivity $K^b_{iso}$ and calculate the diffusivities along the mean gradient and along the isolines of $\overline{b}$.

$$K^b_{iso} = \frac{\psi_0^2}{2} k \overline{f} \mathrm{Re}(i \phi \partial_z \phi^*) |\nabla \overline{b}|^{-1} \tag{2.22}$$

$$\kappa_b = K^b_{iso} \frac{\mathbf{n} \cdot \nabla \bar{b}}{|\nabla \bar{b}|} \; , \; \nu_b = K^b_{iso} \frac{\mathbf{n} \cdot \nabla \bar{b}}{|\nabla \bar{b}|} \tag{2.23}$$

If wavenumber and mean buoyancy gradient are perpendicular, $\nu_b$ would vanish and $\kappa_b = K^b_{iso}$. The eddy vorticity flux can be calculated using equation (2.19)

$$\overline{\mathbf{u}'_h q'} = \overline{\nabla \psi' \cdot \tilde{\beta}/(c - \tilde{U}) \cdot \psi'} = -\frac{\psi_0^2}{2} \frac{\mathrm{Im}(c)|\phi_n^2|}{|\tilde{U} - c|^2} \mathbf{k} \tilde{\beta} \tag{2.24}$$

and vorticity diffusivities by

$$K^{pv}_{iso} = \frac{\psi_0^2}{2} k \frac{\mathrm{Im}(c)|\phi_n^2|}{|\tilde{U} - c|^2} \tag{2.25}$$

$$\kappa_{pv} = K^{pv}_{iso} \frac{(\mathbf{n} \cdot \nabla \bar{q})^2}{|\nabla \bar{q}|^2} \; , \; \nu_{pv} = K^{pv}_{iso} \frac{(\mathbf{n} \cdot \nabla \bar{q})(\mathbf{n} \cdot \nabla \bar{q})}{|\nabla \bar{q}|^2} \tag{2.26}$$

For stable modes the complex part of the phase speed $c$ is be zero, so $K^{pv}_{iso} = 0$. For growing waves ($\omega_i > 0$), vorticity diffusivities are always positive. This is not the case for buoyancy diffusivities.

A crucial point of the closure remains the amplitude $\psi_0$ of the perturbation wave streamfunction. It has to consist of a typical lengthscale and a typical timescale for the eddy circulation.

Following *Killworth* (1997) and *Eden* (2011), the amplitude of the linear solution depends on the imaginary part of the phase speed $c_i = \omega_i / k$ and the wave length $L_{bci} = 2\pi/k$ of the fastest growing mode. By including the growthrate $\omega_i$, the amplitude of the fastest growing waves is largest. *Eden* (2011) also introduces a non-dimensional scaling parameter $K_w$, which is of order one. The scaling parameter is representing the relation between the lengthscale of the instable wave and the final eddy lengthscale. The eddy lengthscale is a result of turbulent processes. It is usually larger than the lengthscale of the instable wave due to the inverse turbulent cascade in the meso-scale regime. In this study $\psi_0 = K_w \, c_i \, L_{bci}$ is used for the amplitude of the perturbation streamfunction, with $K_w = 3$.

## 2.6. Conditions for baroclinic instability

When simplifying equation (2.19) by looking at a pure zonal flow U, it becomes

$$\frac{\partial}{\partial z}\left(\frac{f^2}{N^2}\frac{\partial \phi}{\partial z}\right) + \frac{\phi}{U-c}\left(\frac{\partial \overline{q}}{\partial y} - k^2(U-c)\right) = 0 \tag{2.27}$$

Multiplication with $\phi^*$ and integration over z results in a expression for the imaginary part given by

$$c_i\left(\int_{-h}^{0} \frac{|\phi^2|}{|U-c|^2}\frac{\partial \overline{q}}{\partial y}dz + \left[\frac{f^2}{N^2}\frac{|\phi^2|}{|U-c|^2}\frac{\partial U}{\partial z}\right]_{-h}^{0}\right) = 0 \tag{2.28}$$

with the second part coming from the boundary conditions of equation (2.20). For an instable solution ($c_i > 0$) the term in the bracket has to vanish. Conditions of instability can be clasified as Eady-type, Charney-type and Phillips-type instabilities referring to the works of *Eady* (1949), *Charney* (1947) and *Phillips* (1954). They all focus on different necessary conditions for instability.

- Eady-type instabilities

  Eady considered the case $\frac{\partial \overline{q}}{\partial y} = 0$, a vanishing gradient of potential vorticity and a constant stratification N. This implies a constant vertical shear of the velocity, $\frac{\partial U}{\partial z} = const$. The condition for instability of the Eady problem depends only on the boundary conditions and can be solved analytically. The solution is an overlapping of two boundary trapped waves.

- Charney-type

  If $\frac{\partial \overline{q}}{\partial y} \neq 0$, Charney-type instabilities occur if $\frac{\partial U}{\partial z}$ has the same sign of $\frac{\partial \overline{q}}{\partial y}$ at the surface $z = 0$ or the opposite sign at the bottom boundary $z = -h$. The upper boundary is usually dynamically more important, because velocity shear and PV gradients are higher at the surface. Thus Charney-type instabilities are mostly surface trapped instabilities.

- Phillips-type

  Phillips-type instabilities occur, if the PV gradient $\frac{\partial \overline{q}}{\partial y}$ changes sign in the interior.

Phillips used a two layer model to study these instabilities. In more complex ocean profiles, PV gradients can change several times in different depths.

In the numeric solution, which implements the boundary condition in the mean PV gradient, all three conditions for instability are equivalent to a zero crossing of the gradient. An Eady-type instability therefore is characterised by contributions to the PV gradient at the boundaries of opposite sign, that are the main source of instability. The fictive zero-crossing occurs at middepth. A Charney-type instability is in this case related to a zero crossing of the PV gradient near the surface. To clasify the instability, perturbation waves, which have a streamfunction amplitude that has bottom and surface maxima are called Eady-like instabilities and perturbation waves with an rapidly decreasing amplitude towards depth are called Charney-type instabilities. Instabilities, which are the response of interior crossings of the PV-gradient usually have a surface intensified streamfunction, that decreases slightly with depth. These type of instabilities are here called Phillips-type instabilities.

# 3. Dataset

To produce global maps of instability and diffusivities, the World Ocean Circulation Experiment (WOCE) Global Hydrographic Climatology is used. The WOCE climatology is based on different kinds of observational studies, described by *Gouretski and Koltermann* (2004). It has a horizontal resolution of 0.5° and consists of 44 vertical levels. To remove meso-scale features the data was smoothed with a 1.5° running mean. Geostrophic velocities were computed from the potential density gradients using thermal wind balance with a level of no-motion at the bottom. The results of LSA do not change with a barotropic background current, so the level of no motion could also be defined elsewhere. The topography is taken from the WOCE data and smoothed on 2.5° to remove small scale patterns. The instabilities are calculated on a 1°-grid. The calculated diffusivities are further smoothed with a 3° running mean.

A map of geostrophic velocities is shown in fig.(3.1a) to illustrate the dominant currents. Around the equator, velocities in the real ocean are mostly ageostrophic and can not be expressed by the thermal wind equation. The presented linear stability analysis presumes quasi-geostrophy, so results at ±5° of the equator are masked as the approximations are not valid.

A typical lengthscale for geophysical fluid dynamics is the first baroclinic Rossby radius $L_{Ro}$ shown in fig.(3.1b). The size of $L_{Ro}$ can be calculated by applying the stretching operator on the density-profile without considering background currents (see Appendix A.2). It is the scale of the stable perturbation wave response on an ocean at rest.

The most important variables for baroclinic instability are the vertical shear of geostrophic velocities and the stratification. The Richardson number $Ri = N^2/((\partial_z U)^2 + (\partial_z V)^2)$

a

b

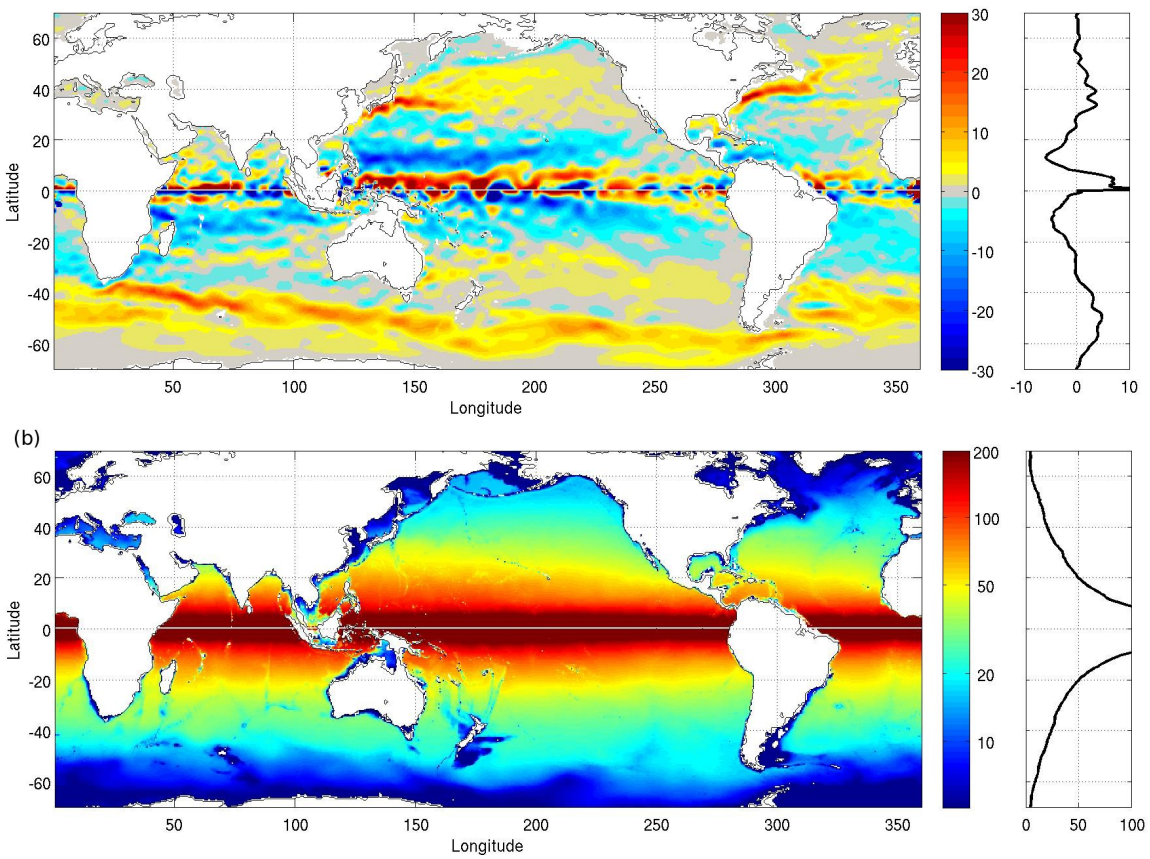


Figure 3.1.: (a) Geostrophic velocities [cm $s^{-1}$] in 150 m depth. (b) First baroclinic Rossby radius $L_{Ro}$ [km]. Zonal means on the right hand side.

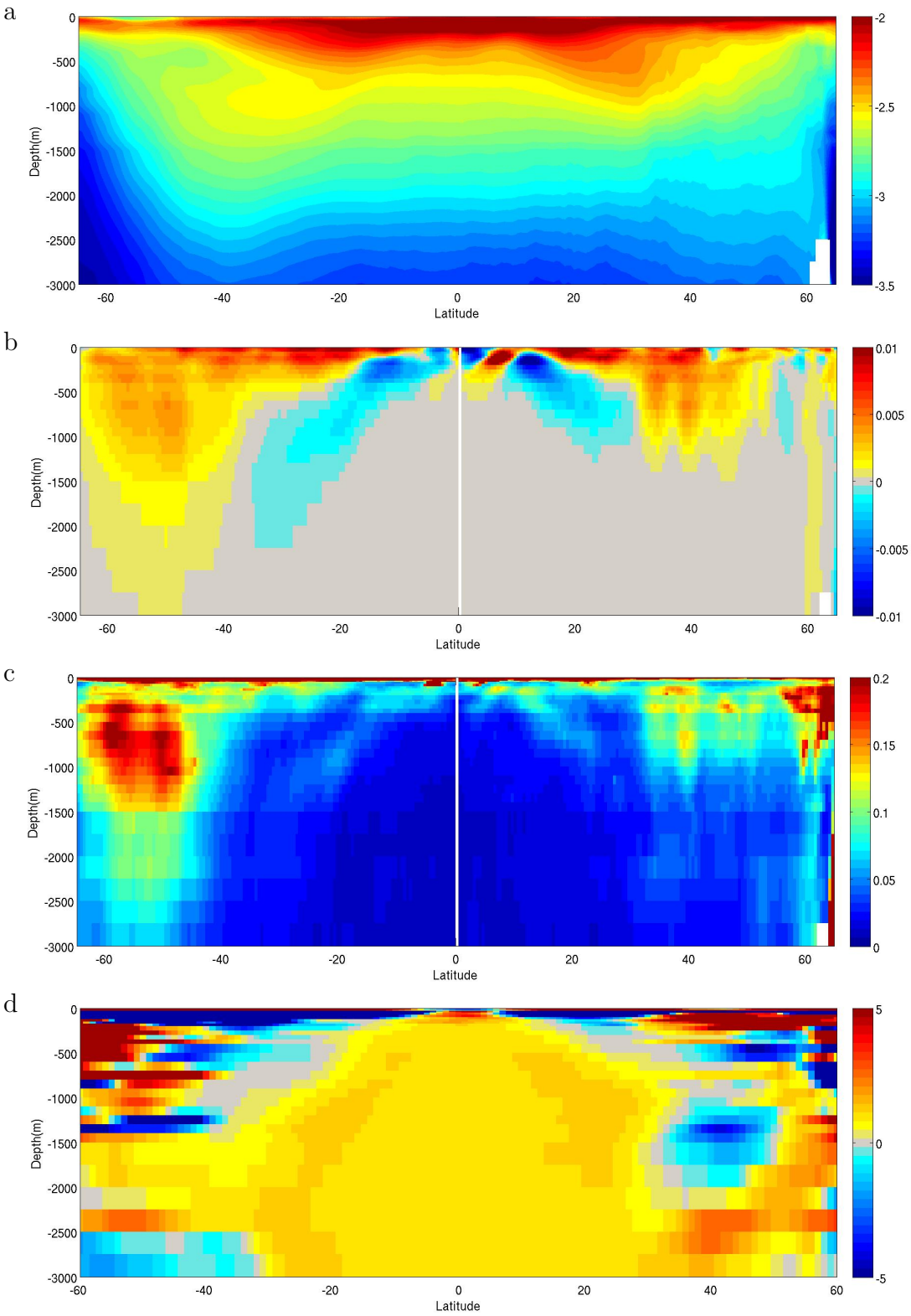


Figure 3.2.: Zonally averaged (a) Logarithm of buoyancy frequency N in $[\lg_{10}(\mathrm{s}^{-1})]$. (b) Vertical shear of zonal geostrophic velocity scaled by the Coriolis parameter $\partial_z \overline{u} \cdot |f|$ in $[\mathrm{s}^{-2}]$. (c) Scaled inverse Richardson number $|f| \cdot \sqrt{\mathrm{Ri}}$ in $[\mathrm{d}^{-1}]$. (d) Meridional PV gradient in units of planetary vorticity $\partial_y \overline{q}/\beta$.

combines the two variables and is a measure for the baroclinic instability of the ocean. Figure(3.2) shows zonal averages of stratification, zonal velocity shear, scaled inverse Richardson number $\sqrt{f^2 Ri^{-1}}$ and meridional vorticity gradient. The dominant flow regimes are apparent in fig.(3.2b). Eastward sheared flow is characterised by positive vertical shear and mixed shear by a reverse of shear in the upper ocean. Vertical shear is positive at the surface with exception of the equatorial region. The scaled inverse Richardson number shown in fig.(3.2c) shows up to two maxima in the vertical, the surface one related to low stratification in the mixed layer and the interior one related to strong shears in the interior. Both maxima are sources for baroclinic instability. The averaged PV gradient also shows a zero crossing beneath the surface and further zero crossings in the interior.

# 4. Results

The Results will be structured as follows. In section one we will look at the instability and the diffusivities from simple profiles. We will start from the conditions Eady solved analytically and add complexity by adding a planetary vorticity gradient, bottom topography and depth-dependent shear successively. In the second section, results for examplary profiles from the WOCE climatology are discussed. In the third section, LSA is applied on the whole WOCE climatology. The horizontal distribution of growthrates and lengthscales of the perturbation waves is shown. The results are compared to a simple approach using the Richardson number and LSA without bottom slopes. In the fourth section, PV- and thickness diffusivities derived from WOCE data are presented. The results are discussed for different regimes and compared with the conclusions drawn from the discussion of idealized profiles.

## 4.1. Idealized Profiles

Before we look at results derived from data, a closer look at the basic concepts and results of the numeric solution is necessary to understand the abilities of the method. Linear stability analysis allows to specify general properties of different current systems. It will be seen, that the latitudinal position and the mean direction of a certain current already delivers a lot of information about the wave solution and the vertical distribution of diffusivities.

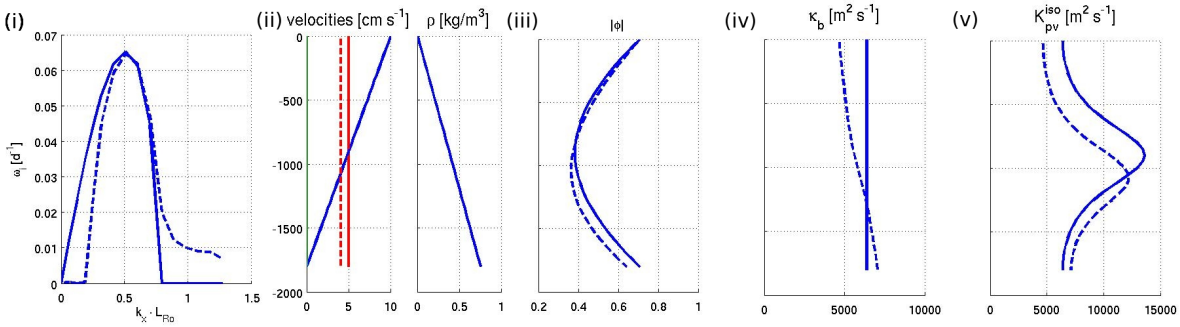


Figure 4.1.: Numeric solutions for the Eady profile without (straight) and with $\beta$ (dashed). Shown are (i) the maximum growthrate $\omega_i$ in dependence of the zonal wavenumber. The wavenumber is scaled by the first baroclinic Rossby radius $L_{Ro}$. (ii) The background velocity U (blue) and the real phase speed c (red) of the perturbation wave, and the background density. (iii) The non-dimensional eigenfunction amplitude of the fastest growing mode. (iv) The thickness diffusivity $\kappa_b$ and (v) PV diffusivity $\kappa_{pv}$ derived from the fastest growing mode. The maximum growthrate is $\omega_i = 0.064\text{d}^{-1} \approx 0.1\frac{U_0}{L_{Ro}}$.

**Eady's conditions** We start with the simple case analytically solved by *Eady* (1949). Eady looks at a pure zonal flow with a constant shear, with the highest velocity $U_0$ at the surface. The stratification is also constant and the planetary vorticity gradient $\beta$ is zero. The numerical solution is shown in fig.(4.1). All long zonal waves with wavenumbers $k_x < 0.76\, L_{Ro}$ are unstable. The most unstable wave with an imaginary growth rate of $\omega_i \approx 0.1\frac{U_0}{L_{Ro}}$ lies at $k_x \approx \frac{0.5}{L_{Ro}}$. Thus the lengthscale of the baroclinic instability wave is $L_{bci} = k^{-1} \approx 2L_{Ro}$. The wave amplitude is largest at the surface and the bottom with a phase shift of 180 degrees between them.

The vertical eigenfunction is a response on the boundary contribution to the potential vorticity gradient at surface and bottom. These contributions to the PV gradient result from the boundary conditions and are of same magnitude and opposite sign in this simple case. To maintain the kinematic condition,

$$\int_{-h}^{0} \overline{\mathbf{u}_h' q'} dz = -\int_{-h}^{0} \kappa_{pv} \cdot \nabla_h \overline{q} = 0 \tag{4.1}$$

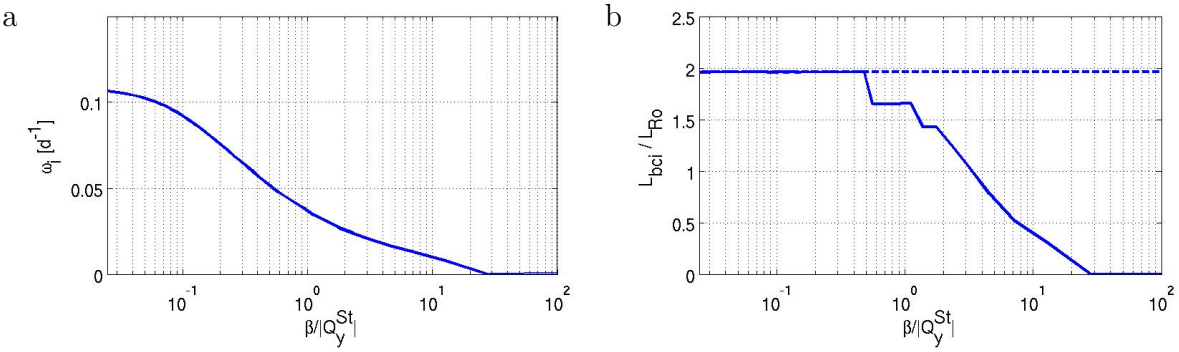


Figure 4.2.: Dependency of (a) Growthrate $\omega_i$ and (b) wavelength $L_{bci}$ of the fastest growing Eady mode shown in fig.(4.1) on the relation between $\beta$ and the approximated stretching vorticity gradient $Q_y^{St}$. The dashed line is the solution for $\beta = 0$.

$\kappa_{pv}$ thus needs to have the same value at surface ($z = 0$) and at bottom ( $z = -h$ ). The most unstable eigenfunction for this condition is symmetric to mid-depth. The kinematic condition (4.1) assures, that the instability process just redistributes momentum and is no source for momentum. The phase speed of the wave is $c = U_0/2$. The resulting thickness diffusivity is vertically constant, the PV diffusivity is symmetric around mid-depth and has a maximum at the so-called steering level, where $U - \mathrm{Re}(c) = 0$.

**Planetary vorticity** The first step towards a more realistic representation of ocean conditions is the inclusion of a planetary vorticity gradient $\beta \neq 0$ as discussed by *Phillips* (1954). The first effect of a nonzero PV gradient is a stabilization of long waves and a destabilization of short waves (see dashed lines in fig.(4.1)). A threshold of vertical shear exists, depending on $\beta$, which needs to be exceeded for an instability to occur. This differs from the Eady-case with $\beta = 0$ , where instability exists as long as velocities are vertically sheared.

The change of properties of the wave solution is a response on the different PV gradient and on the additional Doppler shift of the phase speed by $\beta$. An eastward propagating perturbation wave is slowed down by the planetary vorticity gradient (see fig.(4.1ii)).

As a consequence $U - \mathrm{Re}(c) = 0$ occurs at increased depth, which results in a deeper

maximum of PV diffusivity. The depth integrated meridional PV gradient does not vanish due to the depth-independent $\beta$. To still maintain the kinematic condition in equation (4.1), the PV diffusivity has to increase towards depth. Consequences are a depth intensified wave amplitude and a depth intensified thickness diffusivity. Instability of an eastward mean current would thus lead to an surface intensification of the current as gradients are faster reduced in depth.

For the opposite case of a mean westward current, the $\beta$-contribution leads to a surface intensification of diffusivities and thus a stronger remove of gradients in the upper ocean. The additional Doppler shift increases the westward phase velocity, leading to a near-surface maximum of PV diffusivity. For a meridional mean current with constant shear, the planetary vorticity gradient has no influence on the solution.

The meridional stretching vorticity for constant shear and stratification can be approximated by $Q_y^{St} = f^2/N^2 \cdot U_0/h^2$, with $U_0$ being the velocity at the surface and h the local depth. Figure(4.2) shows how the relation between the stretching and planetary vorticity changes the wave solution. The stretching term decreases towards the equator due to the decreasing Coriolis term $f^2$, while the $\beta$ term increases. Thus the trends shown in fig.(4.2) can be also be interpreted as a lateral dependency of growthrates and lengthscales of the Eady mode.

The decrease of growthrates with latitude can be mainly linked to the decreasing stretching term. The lengthscale on the other hand just depends on the relation between $\beta$ and $Q_y^{St}$. It can be seen in fig.(4.2), that the lengthscale of the wave decouples from the local Rossby radius at the latitude, where $|Q_y^{St}| < \beta$.

As seen in fig.(3.2) the world ocean can be roughly divided in two regimes. A higher latitude regime polewards of about 35 degrees, where strong PV gradients persist through the whole water-column, and a low latitude regime, where the interior PV gradient is close to the planetary vorticity gradient $\beta$, with exception of a shallow surface layer. From this simple example one would expect wave solutions with a wavelength linked to the Rossby radius for the higher latitudes and solutions with wavelengths decoupled from the Rossby radius in low latitudes. Although the PV gradients in the ocean are a

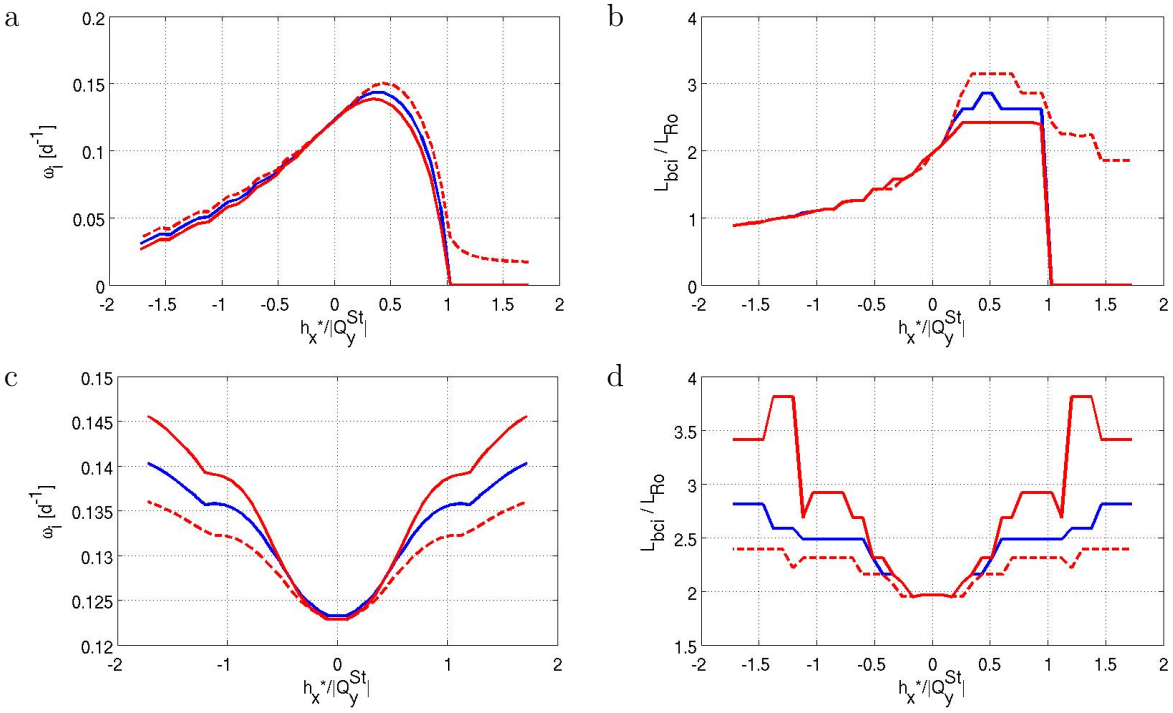


Figure 4.3.: Dependency of (a,c) Growthrate $\omega_i$ and (b,d) wavelength $L_{bci}$ of the fastest growing Eady mode on the contribution of the (a,b) cross-stream topographic slope $h_y^*$ and (c,d) the along-stream topographic slope $h_x^*$ normalized by the approximated stretching-PV gradient $Q_y^{St}$. Eastward Flow $U > 0$ and $\beta = 0$ (blue). Eastward Flow $U > 0$ and $\beta \neq 0$ (red). Westward Flow $U < 0$ and $\beta \neq 0$(red dashed).

lot more complex than Eady conditions, we will see that the decoupling from the Rossby radius is also observed in the full analysis.

**Sloping topography** Topography plays an important role for the mean ocean circulation, as all non-zonal currents are flowing along a topographic boundary. It also plays a role in the instability of a current. Perturbation waves can no longer propagate freely but are constraint by a horizontal boundary. In the local problem it is not trivial to include topographic constraints. The condition for the local approximation is that the ocean is horizontally homogeneous. A way to include a topographic constraint is to change the lower boundary condition from a vanishing vertical velocity to a vanishing

velocity perpendicular to the bottom slope. Following *Smith* (2007) the bottom boundary condition can also be included in the potential vorticity of the bottom layer. (see Appendix A.5)

In the simple Eady case without a planetary vorticity gradient, a topographic contribution to the PV gradient of $h_y^* = h_y \cdot f/h \geq Q_y^{St}$ would prevent a zero-crossing of the PV gradient and consequently prohibit an instability to arise (see fig.(4.3a)). A slope of $h_y^* > 0$ corresponds to a topographic obstacle at the left side of the current on the northern hemisphere and on the right side on the southern hemisphere.

A topographic slope in the opposite direction reduces growthrates and lengthscales almost linearly and is approaching stability at around $h_y^* <= -3 \cdot Q_y^{St}$, but has no critical value for which the growthrate vanishes. An interesting feature of the numeric solution is, that the growthrate is not highest for a flat bottom, but for a slightly sloping bottom of around half the interior PV gradient. In this domain wavelengths are also larger than for a flat bottom and consequently diffusivities have a higher amplitude as $\kappa \sim \phi_0^2 \sim \omega_i^2 L_{bci}^2$.

When reversing the current direction, instability waves can arise above the critical point of $h_y^* \geq Q_y^{St}$. These weakly growing waves are a response of the zero crossing between the negative surface PV gradient and the positive interior PV gradient caused by $\beta$.

A topographic slope $h_x$ along the zonal mean current always leads to a further destabilization of the flow as shown in fig.(4.3c). In case of an along-stream topographic slope the solution is independent of the slope's sign. An obstacle upstream would result in the same change of properties of the instable wave as an obstacle downstream. The increase of growthrate and lengthscale by an along-stream topographic slope is larger for westward currents.

Studying Eady's condition under influence of a planetary PV gradient and topographic boundary conditions reveals, that the values predicted by Eady for growthrate and lengthscale are indeed valid for a constant interior PV gradient large in relation to $\beta$ and $\nabla h^*$. Both parameters however are able to significantly change the magnitude of growthrate and lengthscale of the perturbation waves, if they are larger or at comparable

value to the PV gradient.

**Depth-dependent PV gradients** As neither shear nor stratification are constant in the ocean, PV gradients have a much more complex structure than the constant or vanishing PV gradients in the Eady problem.

A still idealized ocean profile would consist of a strongly sheared and strongly stratified upper ocean and a weakly sheared and weakly stratified lower ocean. This can be approximated by exponential functions. Some differences to the constant cases can be found and need to be explained to better understand the effects in the real ocean.

Figure(4.4a) shows eastward and westward mean flow. The instability of the eastward current produces similar diffusivities as the Eady mode, the instability of the westward current produces surface-intensified diffusivities. The growthrate of the westward current is almost twice as large as the growthrate of the eastward current. From the different vertical distributions of thickness diffusivity it becomes evident, that the baroclinic instability process tends to produce surface intensified eastward zonal currents and bottom intensified westward zonal currents. These currents are the most stable. On the other hand bottom intensified eastward currents and surface intensified westward currents are highly unstable. Examples in the real ocean are the Gulf Stream and Kuroshio extensions for surface intensified eastward mean currents. The subtropical westward return currents are examples for surface intensified westward mean currents.

Northward and southward currents (fig.(4.4b)) produce equal time- and lengthscales of instable waves. The growthrate is independent of the direction, because the contribution by the planetary vorticity gradient is perpendicular to the flow. The diffusivities are also equal. The difference in the meridional profiles is, that skewness diffusivities $\nu_b$ and $\nu_{pv}$ are created by the instability.

Skewness diffusivities lead to an advection of properties along the mean isopycnal layers. These diffusivities are induced, when the wave propagation is not perpendicular to the mean gradients of either buoyancy or PV, as shown in equations (2.23) and (2.26). In the simplified case shown in fig.(4.4b), the angle between mean buoyancy gradient and wave propagation is a result of the vanishing interior zonal PV gradient at depth and

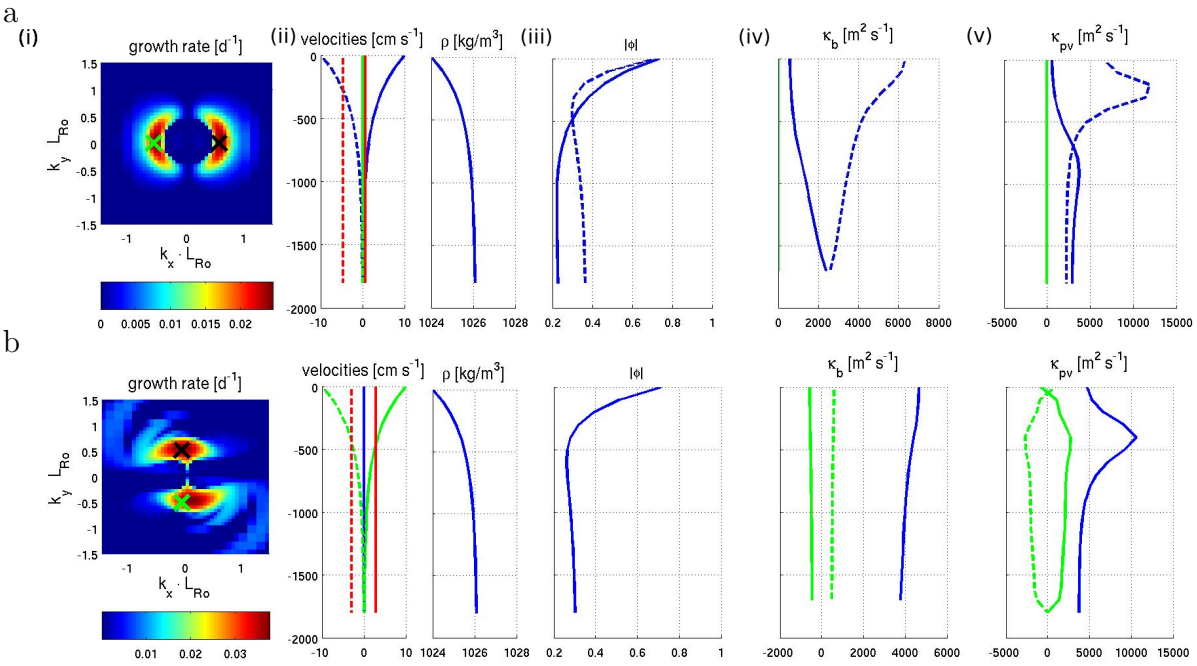


Figure 4.4.: Numeric solutions for four different idealized current profiles.(a) Zonal Currents. (b) Meridional Currents. Shown are (i) the maximum growthrates $\omega_i$ in horizontal wavenumber space. The wavenumbers are scaled by the local first radius of deformation $L_{Ro}$. The black (green) cross marks the fastest growing mode corresponding to the straight (dashed) lines in the other plots. The maximum growthrates are $\omega_i = 0.025\text{d}^{-1}$ (eastward), $\omega_i = 0.041\text{d}^{-1}$ (westward) and $\omega_i = 0.038\text{d}^{-1}$ (north/southward)(ii) The background velocities U (blue) and V(green), the real phase speed c (red) of the perturbation wave and density . (iii) The non-dimensional amplitude of the vertical eigenfunction of the fastest growing mode. (iv) The thickness diffusivity $\kappa_b$ and (v) PV diffusivity $\kappa_{pv}$ (blue) and skewness diffusivities $\nu_b$, $\nu_{pv}$ (green) derived from the fastest growing mode.

the constant meridional gradient $\beta$.

The vertically changing relation between interior PV gradient and $\beta$ lead to a slight rotation of the direction of the total gradient with depth. In profiles of increased complexity the vertical rotation of the PV gradient can also originate from depth dependent meridional and zonal velocities. The isopycnal thickness advection $\nu_b$ is creating a meridional mean buoyancy gradient and thus inducing a zonal mean current and a zonal eddy-induced advection. The instability of northward and southward currents would both lead to an eddy-induced advection towards east, a consequence of the planetary vorticity gradient.

## 4.2. Profiles from observational data

In the ocean, *Tulloch et al.* (2011) claim that most baroclinic instabilities can be identified as Philips-type instabilities, that means the PV gradient has a sign-change in the interior, and that Charney instabilities, which represent subsurface or shallow sign-changes, are only dominant in westward mean flows. Analogous to their work different profile-types from the WOCE climatology are chosen to show the influence on the solution of LSA.

**Antarctic Circumpolar Current profile** The first profile shown in fig.(4.5a) is a profile from the ACC (53° S, 150° W), representing mean eastward flow. The conditions in the ACC are close to Eady's conditions as shear and stratification have a low vertical dependence. The instability impacts the whole water column, the thickness diffusivity is almost constant and the PV diffusivity increases towards depth with a local maximum at the steering level. The lengthscale of the wave is almost equal to the lengthscale $L_{bci} \approx 2L_{Ro}$ of the Eady solution. The topographic slope has a large influence on the growthrate and the magnitude of diffusivities. Figure(4.6) shows the dependence of growthrate and lengthscale of this specific profile on the local slope. Like the Eady profile, the mean eastward current is stabilized by a topography sloping towards the

right side of the current.

**Gulf Stream profile** The profile from the GS (37.5° N, 61.5° W) shown in Fig.(4.5b) is characterised by strong zonal and meridional velocities. The zero-crossing of the PV gradient is at a lower depth. The lengthscale is a little smaller than the Eady-scale, but still close. The diffusivities are similar to the ones shown in fig.(4.4b) for a pure northward flow. As meridional currents are not stabilized by the planetary PV gradient, they tend to dominate in the instability process, if they have a similar magnitude as the zonal eastward velocity. Like on the ACC profile, the topographic stabilization has a large effect. As shown in fig.(4.6), the current is also stabilized by a slope perpendicular to the current-axis.

**Mixed shear profiles** Figure(4.5c) shows a profile for a mixed shear (15° S, 180° E). The dominant zonal velocity is concentrated in the upper 1000 m, the buoyancy gradient beneath is almost zero. The velocity shear and the PV gradient change sign at approximately 150 m depth. Two different maxima in the wavenumber space indicate two different types of growing solutions . Dominant in this profile is a wave-solution with a lengthscale several times smaller than the local Rossby radius. The vertical eigenfunction shows, that this wave has an amplitude confined to the upper 200 m. The instability can either be attributed to the near-surface zero crossing of the PV gradient or to an interaction of the interior PV gradient with the surface gradient. Diffusivities are also vanishing underneath 200 m and are one order of magnitude smaller than in the profiles from the ACC and the Gulf Stream.

A comparison with a profile, where the large scale instability is dominating (see fig.4.5d), shows that the mode in fig.(4.5d) is related to the interior zero-crossing (Phillips-type) and the mode in fig.(4.5c) to the interaction with the surface gradient (Charney-type). The diffusivities from the Phillips-type instability are much larger than from the Charney-type instability. Depending on wich mode dominates, diffusivities may vary in one order of magnitude. This explains a lot of the noise to be observed in the global maps. Topographic slopes have very little influence on the two equator-near profiles.

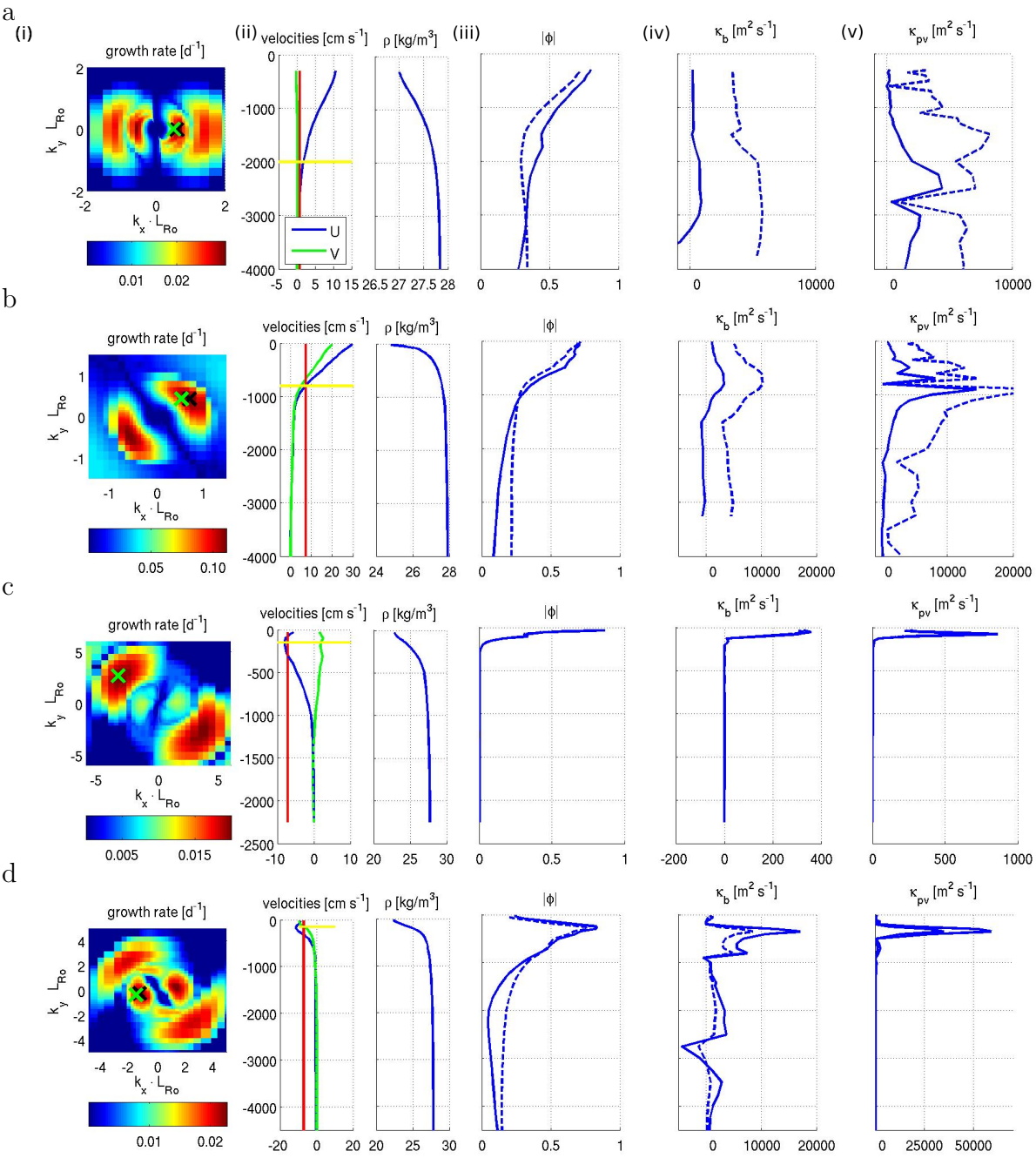


Figure 4.5.: LSA solution for profiles from WOCE data at (53S/150W), (37,5N/61.5W), (15S/180E), (15N,180E). Properties shown are the same as in fig.(4.4). The black(green) cross marks the pair of wavenumbers with maximum growthrate with(out) a flat bottom boundary condition and the straight(dashed) lines mark the derived properties. The red line in the velocity profile marks the zonal phase-speed and direction of the perturbation wave. The yellow line marks the depth of the approximate zero-crossing of the meridional PV gradient.

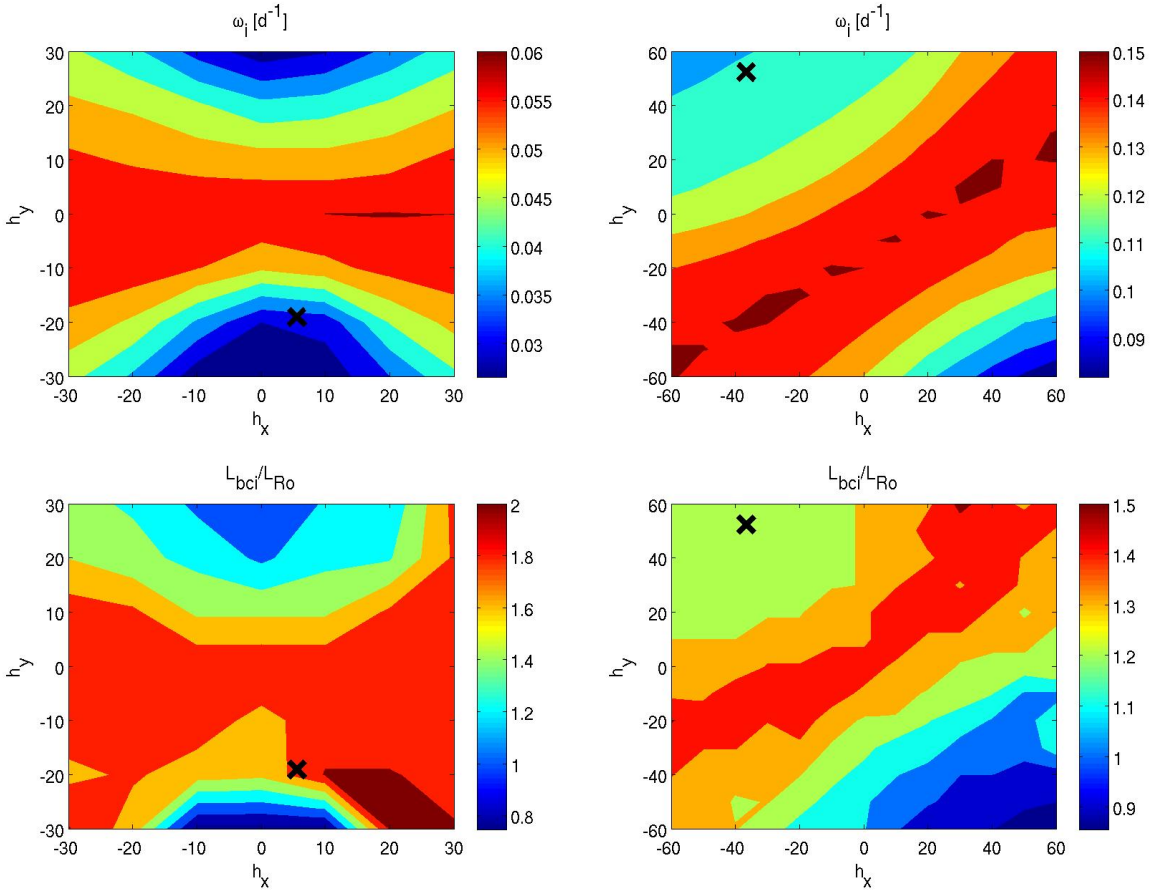


Figure 4.6.: Dependency of growthrate (top) and lengthscale (bottom) on the local topographic slope $\nabla h$ $[10^{-2}\%]$ of the ACC profile shown in fig.(4.5a) (left) and the GS profile of fig.(4.5b) (right).The cross marks the real topographic slope.

## 4.3. Global eddy lengthscales and growthrates

The magnitude of eddy diffusivities is directly linked to the growthrate and the lengthscale of the fastest growing mode. The idealized profiles in the first part of the results reveal the important variables for these two wave-properties . In the Eady profile the magnitude of the stretching PV gradient $Q_y^{St}$ is important for the growthrate and the relation between $\beta$ and $Q_y^{St}$ is important for the lengthscale. For a depth-dependent PV gradient, $\beta$ has an influence on the growthrate as well. Surface intensified eastward sheared profiles are more unstable than surface intensified westward sheared profiles. Another variable that determines the magnitude of growthrate and lengthscale of the fastest growing mode is the topographic slope. A topographic slope can either stabilize or destabilize the background current. Example profiles from the WOCE climatology further show that the complex structure of PV gradients in real ocean profiles can cause the growth of different modes. These different modes usually have different lengthscales and vertical eigenfunctions and can be roughly divided into Charney-type, Phillips-type and Eady-type modes.

To understand how the different variables influence growthrates and lengthscales on a global scale, we apply linear stability analysis on the whole WOCE climatology. We computed results with and without a bottom contribution of the local topographic slope to receive information about the dependency on the slope.

Furthermore we compare the results from LSA with the approximated Eady growthrate for non-constant shear and stratification and with an approximate lengthscale. The difference between the three different results visualizes the consequences of increased complexity arising from zero crossings of the PV gradient, planetary vorticity and topographic stabilization. The approximate solution is chosen, because it represents a popular method to receive time- and lengthscales for baroclinic instability with low computational effort.

Fig.(4.7a) shows the global map for the maximum growthrate retrieved with linear stability analysis. The most unstable areas are along the Antarctic Circumpolar Current and along the mayor boundary currents. Other unstable spots can be located in the

polar North Atlantic. The lengthscale of the fastest growing mode is shown in fig.(4.8a). The noisiness of the horizontal dependency of lengthscales is a result of the different dominant modes of different lengthscale as seen in the fig.(4.5). The zonally averaged values actually provide a better overview over consistent features. Lengthscales of unstable waves are larger than the Rossby radius polewards of 40-50 degree and much smaller towards the equator. Fig.(4.10) shows that the zonal mean lengthscale is quite constant and lies between 10 and 20 km polewards of 20 degree. Between 20 and 10 degrees the lengthscales have a local maximum, which can be linked to mixed shear return currents of the subtropical gyres.

**Influence of topography** The maps of growthrate (fig(4.7b))and lengthscale (fig(4.8b)) that result for LSA with flat bottom show a systematic modification to the full solution. Fig.(4.9) shows the differences between the two results. As seen in the example profiles in fig.(4.5) the inclusion of a topographic slope in the lower boundary condition leads in most cases to a suppression or weakening of growing modes. The effect is strongest in the ACC, where large areas of the mean current seem to be stabilized by topography. In the northern hemisphere most notably the Labrador current and the Gulf Stream become more stable. Zonally averaged growthrates and lengthscales show that topographic slopes have the largest influence polewards of 40 degree. In this region growthrates and lengthscales are reduced by an average of 10-20 percent. In mid- and low latitudes on the other side, topography often leads to a slight increase of growthrate and lengthscale. This indicates that the relation between interior PV gradient and topographic gradient is in the area, where $0 < \nabla h^* < \nabla Q^{St}$ or that the mean flow faces obstacles along its mean direction.

**An approximate solution** Following *Smith* (2007) the Eady growthrate

$$\omega_E^2 = \frac{1}{h}\int_{-h}^{0} (f^2 Ri^{-1})/6 \, dz$$

can be estimated using the local Richardson number. The Eady growthrate is the growthrate of the fastest growing Eady mode, that is the wave solution for depth-

a

b

c

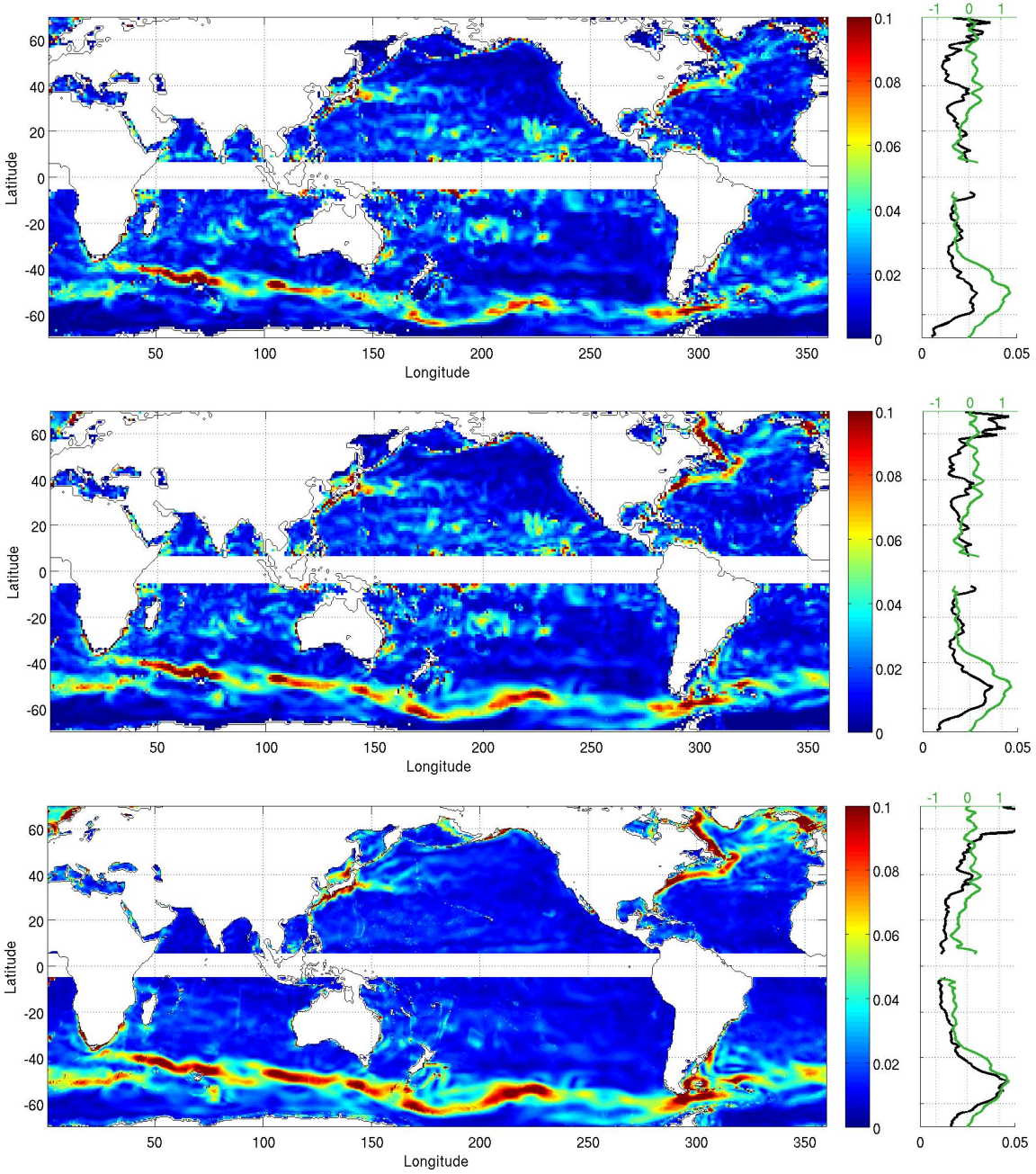


Figure 4.7.: (a) Maximum growthrates $\omega_i$ [$d^{-1}$] from LSA. (b) Same but for a local flat bottom (c) Eady growthrate $\omega_E$. On the right hand side: zonally averaged growthrates (black) and depth averaged zonal mean geostrophic velocities [$cms^{-1}$] (green).

a

b

c

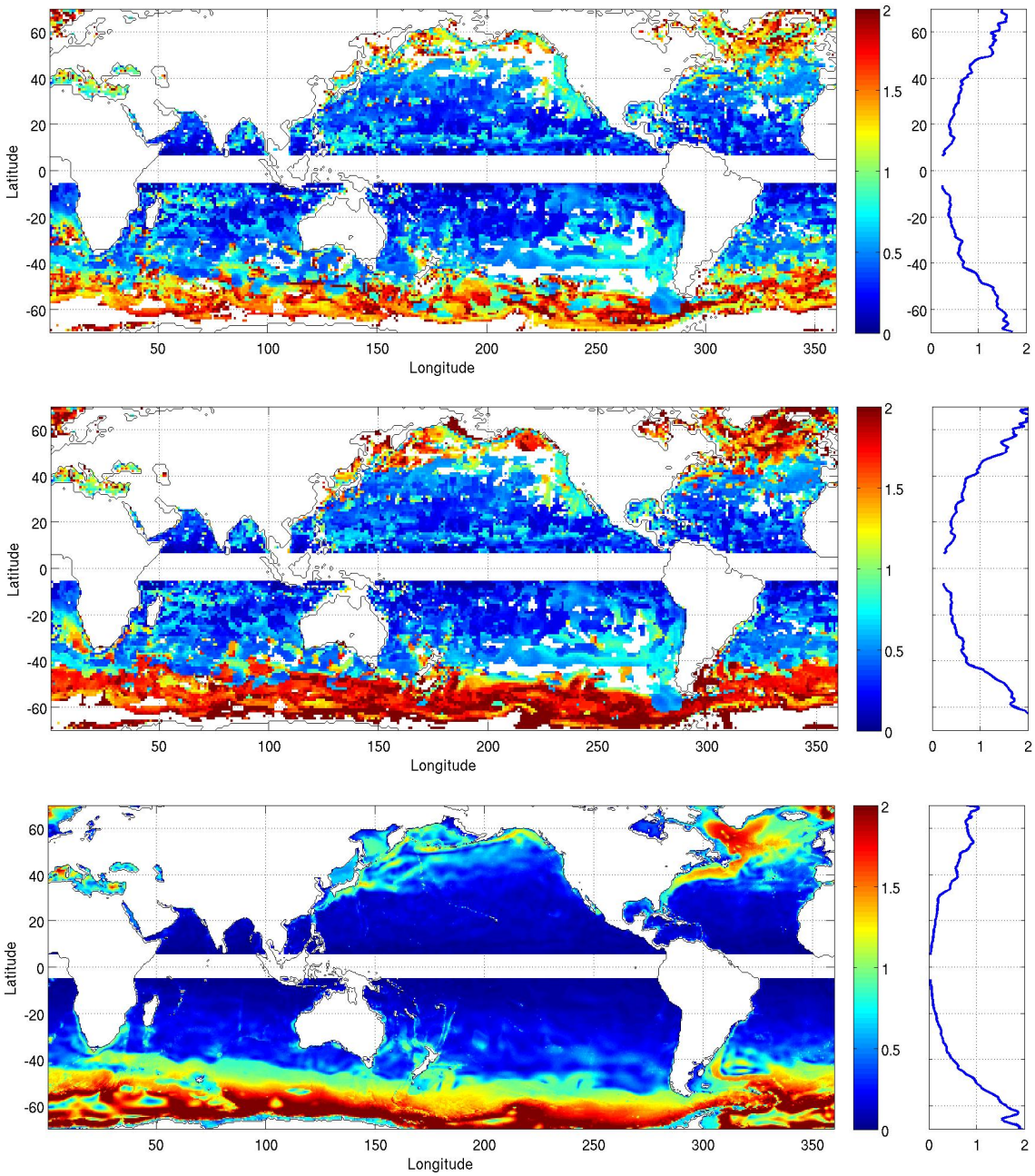


Figure 4.8.: (a) Scaled radius $L_{bci}/L_{Ro}$ of the fastest growing mode and the zonal mean. (b) Same but for a local flat bottom (c) Scaled approximate lengthscale $L_{bc}$.

a

b

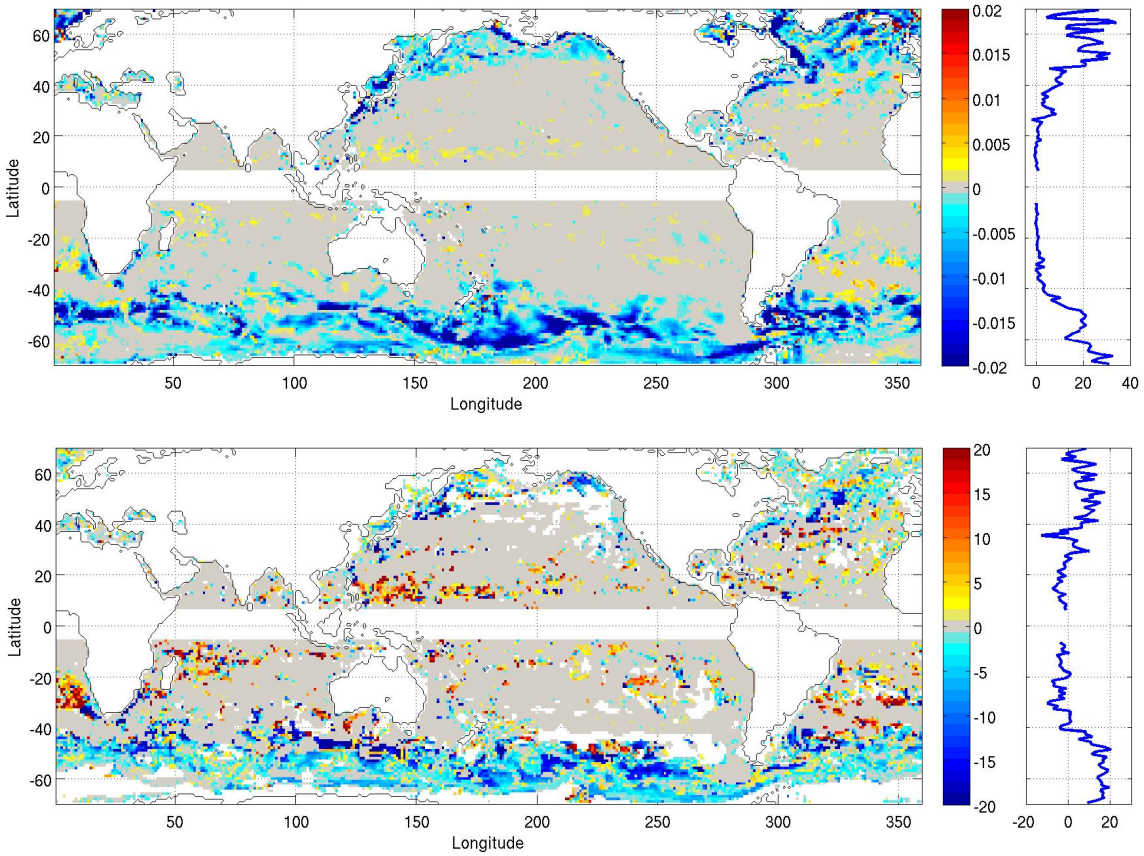


Figure 4.9.: Difference between the solution of LSA with flat bottom shown in fig.(4.7a,4.8a) and the solution with real topography shown in fig.(4.7b,4.8b). (a) Max growthrate [$d^{-1}$].(b) Wavelength of fastest growing mode [km]. Positive(negative) values denote an increase(decrease) by adding sloping bottom boundaries. On the right hand side are zonal mean reductions in percent of the value for a flat bottom.

averaged shear and stratification. The vertical structure of the Eady mode is shown in fig.(4.1).

The growthrate of the Eady mode is neither modified by the influence of topography nor by the influence of $\beta$. However, the Eady growthrate is often used to quantify baroclinic instability in the ocean because it requires little computational effort. By comparing the Eady growthrate with the growthrate from linear stability analysis, we can quantify improved display of baroclinic instability by LSA.

The Eady growthrate is shown in fig.(4.7c). It can be best compared to fig.(4.7b), as we already discussed the influence of topographic slopes, that is the difference between fig.(4.7a) and fig.(4.7b).

Overall the Eady growthrate seems to be a good approximation for the LSA-growthrate. The regions of highest growthrate agree. The systematic difference can be best seen in the zonally averaged growthrates. The Eady growthrates are higher in high latitudes and lower in low latitudes. This difference can probably be largely explained by the influence of the $\beta$-effect on surface intensified shear as shown in fig.(4.4a).

The consequences of the $\beta$-effect are a zonal mean reduction of the growthrate by around 20% in the eastward current regimes polewards of about 40 degrees and an increase by around 50% in the westward currents equatorwards of 25 degrees. The different depth dependencies of shear and stratification in these two regime certainly influence the magnitude of the difference between Eady- and LSA growthrates as well, but the influence of the $\beta$-effect gives already a well-defined explanation.

To calculate an amplitude of eddy diffusivities from approximated values, we are also in need of an approximated lengthscale.

An estimate of the baroclinic instability lengthscale is the eddy transfer length $L_{bc}$. Following *Eden* (2007) $L_{bc}$ can be properly represented by the minimum of the first baroclinic Rossby radius of deformation $L_{Ro}$ and the Rhine's scale $L_{Rhi}$.

$$L_{bc} = \min(L_{Ro}, L_{Rhi})$$

The Rhine's scale normally depends on the eddy kinetic energy. For unknown eddy kinetic energy, it can be approximated by $L_{Rhi} = \omega_E/\beta$ (*Liu et al.* (2012)). The eddy

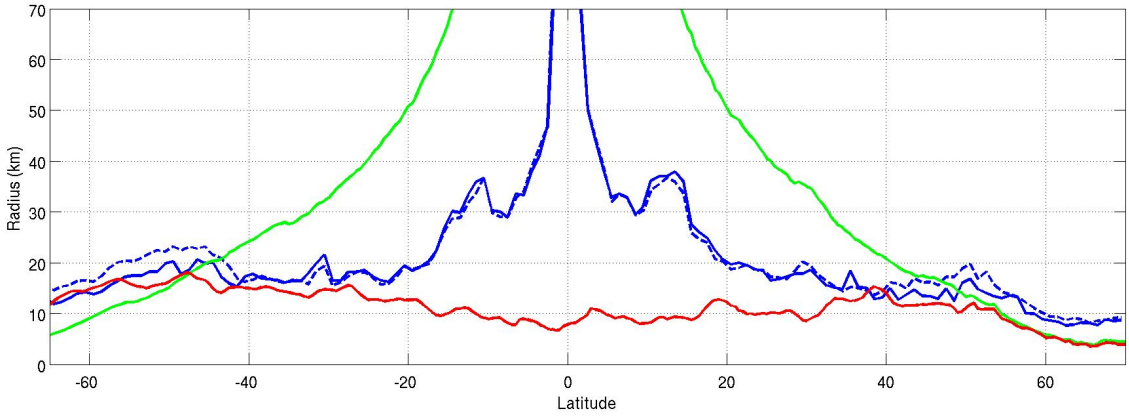


Figure 4.10.: Zonally averaged lengthscales of the local first baroclinic Rossby radius $L_{Ro}$ (green). $L_{bci}$ from LSA with bottom slopes (straight blue). $L_{bci}$ from LSA with flat bottom (dashed blue). The approximate solution $L_{bc}$ (red).

transfer length is shown in fig.(4.8c).

We see that the overall relation between the lengthscale and the baroclinic Rossby radius is similar to the one received with LSA. The horizontal distribution is much smoother than the lengthscale from LSA, because the switch between different modes with different wavelength does not occur. As shown in fig.(4.10) the lengthscale $L_{bc}$ is an underestimation of the lengthscales from LSA in low latitudes, but fits quite well in high latitudes.

We can combine both Eady growthrate and eddy transfer length to calculate the amplitude $\psi_0$ of eddy diffusivities. The main consequence for the amplitude $\psi_0$ of eddy diffusivities would be a large overestimation in high latitudes and an underestimation in low latitudes in comparison to an amplitude constructed with the time- and lengthscales from LSA.

## 4.4. Eddy diffusivities

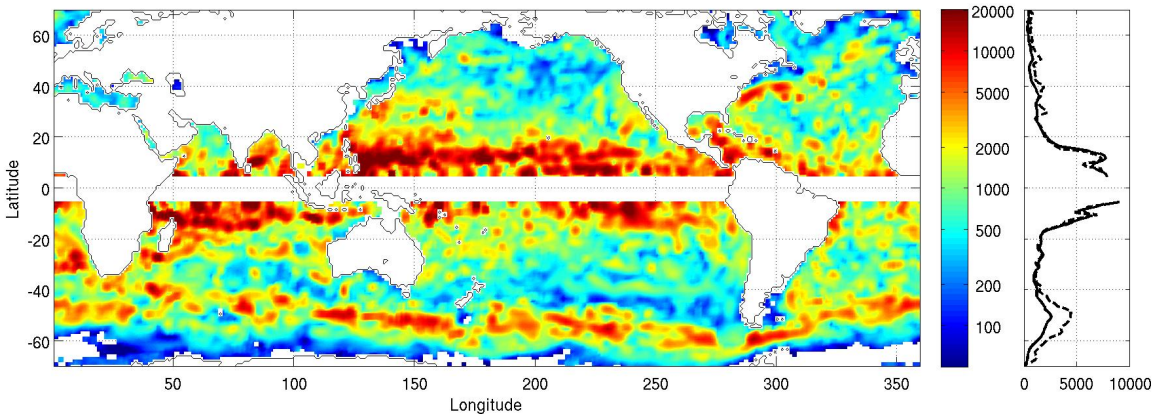


Figure 4.11.: Amplitude $\psi_0$ [$m^2 s^{-1}$] of the streamfunction of the fasted growing wave. Note the nonlinear color axis. On the right hand side are zonally averaged values compared with zonally averaged values for the flat bottom case (dashed line).

In the following section, eddy diffusivities are calculated according to equation(2.23) and equation(2.26) for the WOCE climatology using the results from LSA with topographic slopes. Recent closures are based on the Eady growthrate and an approximate lengthscale and are either vertically constant (*Visbeck et al.* (1997)) or relate the vertical dependency to the Richardson number (*Eden and Greatbatch* (2008)). The advantage of eddy diffusivities computed with LSA is not only the inclusion of $\beta$ and topographic stabilization, but also different depth-structures for PV diffusion and thickness diffusion. LSA also delivers the direction of the wave propagation, that allows to specify the skewness diffusivities $\nu_b$ and $\nu_{pv}$.

All diffusivities depend on the amplitude $\psi_0 = 2\pi K_w c_i L_{bci}$ of the perturbation streamfunction and differ only in their vertical structure. The magnitude of $\psi_0$ is shown in fig.(4.11). The amplitude is largest in the westward currents between 10° and 20°, linked to the larger lengthscale in this region rather than to large growthrates. In the subtropical and subpolar ocean, where the lengthscales are quite constant, areas of a large amplitude are linked to areas of high growthrate, for example in the GS and along

the ACC. In the following sections the detailed vertical distribution of meso-scale eddy diffusivities will be shown on maps for certain depths and for chosen transects.

### 4.4.1. PV diffusivity

Figure(4.12) shows PV diffusivity in 150 m, 500 m and 1500 m depth. Even though growthrates in the Gulf Stream and the Kuroshio are high, the diffusivities are quite low. On the other hand diffusivities in the Southern Ocean are high coinciding with high growthrates. Some areas in the ACC are characterized by higher diffusivities These areas are downstream of South Africa in the Agulhas return current, south of Australia, and in the southern Pacific Ocean. In low latitudes the dominant feature is the high PV diffusivity in the westward current regimes. High diffusivities in the subsurface layers are apparent in the westward equatorial currents of the Indian ocean, of the Pacific and of the North Atlantic.

The absolute influence of topography is largest in the ACC and in the subtropical and subpolar ocean of the northern hemisphere (see zonal averages in fig.(4.12)). In the northern hemisphere topographic suppression is large in the boundary currents, with the largest influence north of 50 degree in the Labrador current. The vertical structure of the zonally averaged $\kappa_{pv}$ is shown in fig.(4.14). The zonal mean diffusivities in the eastward sheared ACC have a mid-depth maximum approximately at the steering level, where $|\mathbf{u}_h - \mathrm{Re}(c)| = 0$ and show an overall increase towards depth.

As seen in the chosen profile from the ACC (see fig.(4.5a)), this structure is close to the Eady-case. The mean steering level gets shallower towards the equator and is deepest in the Southern Ocean. The strong diffusivities north and south of the equator are concentrated in the upper 500 m and can be linked to the westward shear areas of the zonal velocity.

The relation between mean velocities and the resulting PV diffusivity can be best seen in the transects shown in fig.(4.16) and fig.(4.17). In the deep reaching eastward ACC currents, PV diffusivities are often almost constant with an increase towards depth. The increase at the steering level is little and the main effect of the background velocity

on the vertical structure is a suppression of PV diffusivity towards the surface. This behavior corresponds to the Eady mode.
In the Kuroshio and the Gulf Stream $\kappa_{pv}$ is small. The highest values exist around the steering level. Away from the steering level, the suppression by the mean flow is large. In comparison to the ACC, the boundary currents are much more surface-intensified. As discussed in chapter 4.1, surface intensified eastward currents are more stable than deep eastward currents. The small diffusivities in the extensions of the boundary currents are most probably a consequence.

### 4.4.2. Thickness diffusivity

As seen in the previous section, the vertical structure of PV diffusivity is mainly influenced by the depth of the steering level. Thickness diffusivity has no direct dependence on the depth of the steering level. However, as we have seen in the idealized profiles, the vertical structure of thickness diffusivity is similar to the vertical structure of PV diffusivity. Fig.(4.13) shows the global structure of thickness diffusivity at the same depth levels as shown for PV diffusivity. The dominant features are also the low latitude return currents and the ACC. However the boundary currents are more pronounced in comparison to fig.(4.12), especially the Benguela current and the GS. The horizontal distribution is smoother than the distribution of PV diffusivity. At increased depth the GS is characterised by a negative $\kappa_b$, thus an upgradient diffusion of buoyancy. The profile in fig.(4.5b) showed, that this can be related to the influence of topography and occurs underneath the main current.
Negative thickness diffusivity can only exist in our solution, if $\kappa_b$ changes sign in the interior. Depth integrated thickness diffusivity is always larger than zero. Apart from the GS, negative thickness diffusion is apparent in mixed shear regions in low latitudes. The differences between the zonally averaged thickness diffusivity in fig.(4.15) and the zonally averaged PV diffusivity are a more vertically constant distribution in the ACC, with values increasing towards depth and more evenly distributed values in the upper 500 m in low latitudes. Both differences origin from the sharpening of PV diffusion

around the steering level. In the meridional transects the principal similarity of both diffusivities is also noticable. The transect in the GS shows that the sign-change of $\kappa_b$ occurs approximately at 1500 m depth.

a

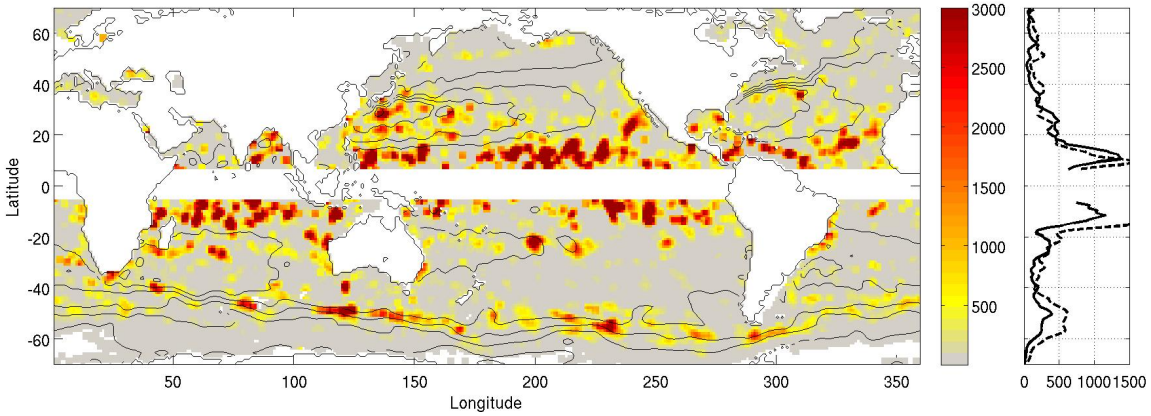


b

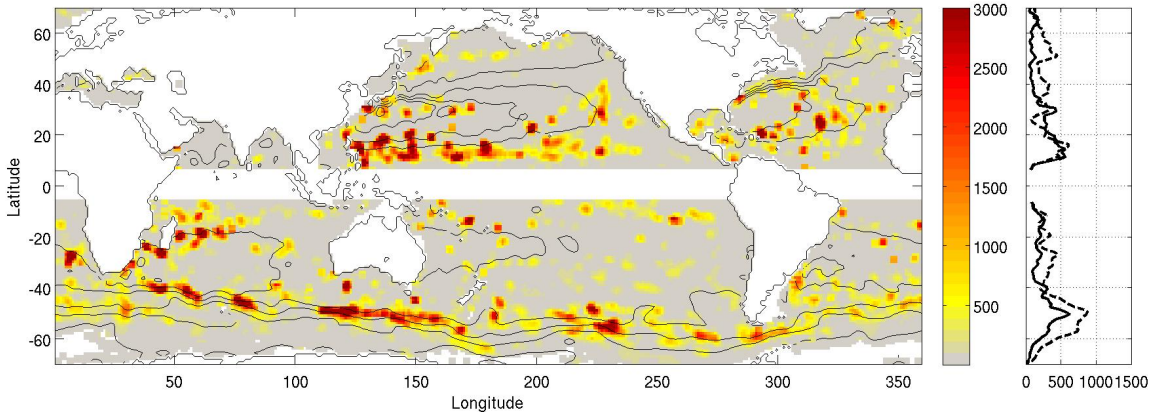


c

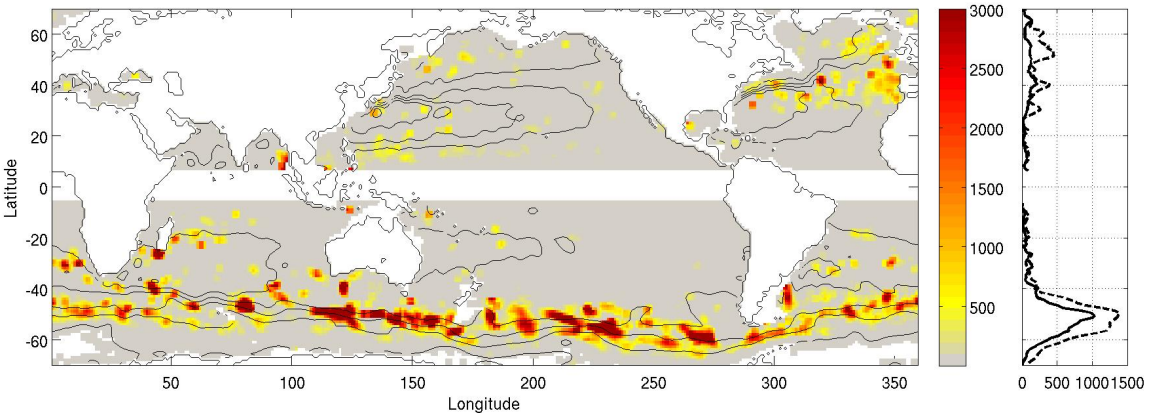


Figure 4.12.: PV diffusivity $\kappa_{pv}$ [$m^2 s^{-1}$] at different depth levels. a) at 150 m. b) at 500 m. c) at 1500 m. Straight lines represent mean buoyancy contours at 500 m depth. On the right side are the zonal means. Straight lines are from the maps shown left and dashed lines are from the respective values for the flat bottom case.

a

b

c

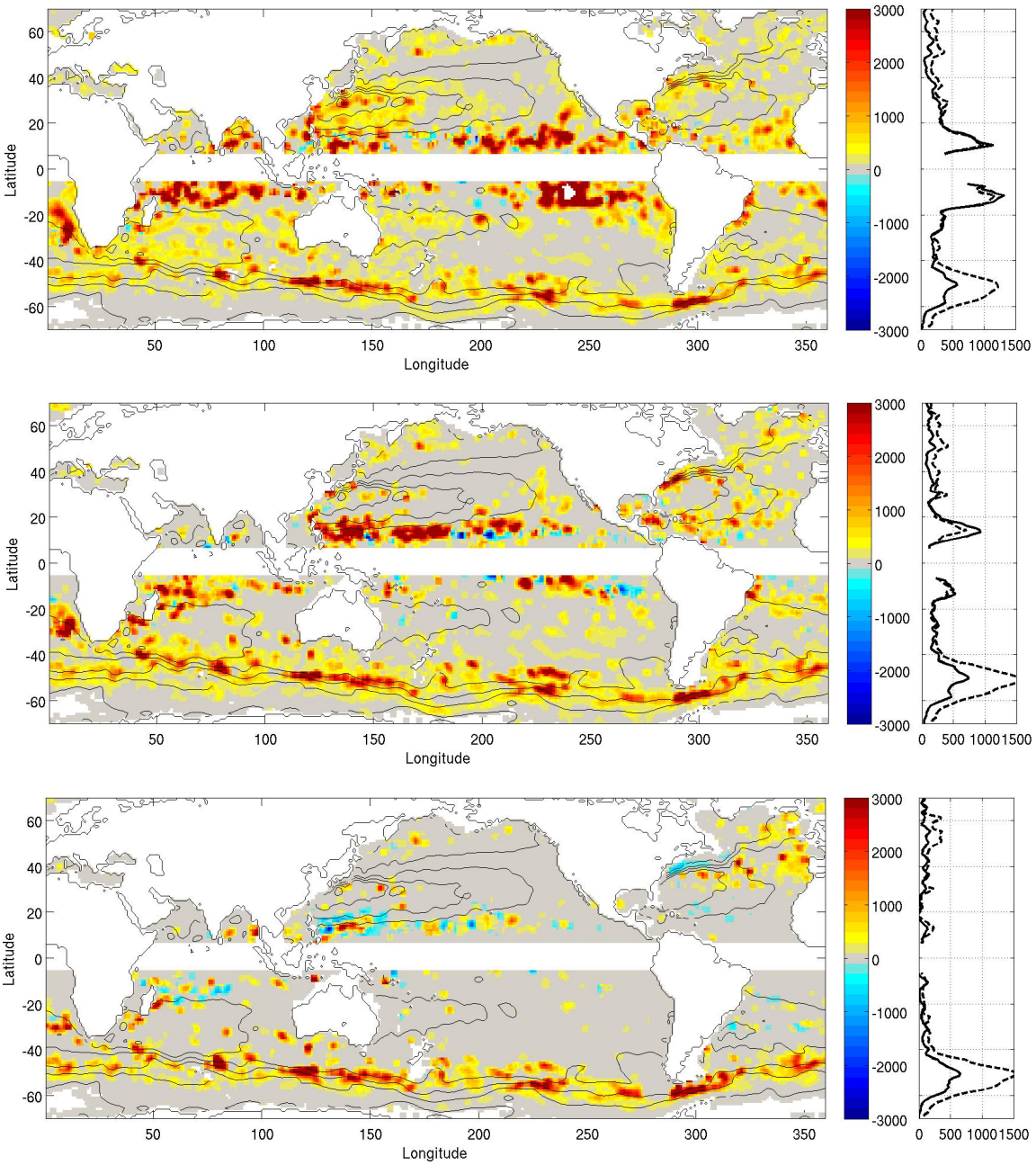


Figure 4.13.: Global maps as in fig.(4.12) but for thickness diffusivity $\kappa_b$ [$m^2\,s^{-1}$] in (a) 150 m. (b) 500 m. (c) 1500 m depth.

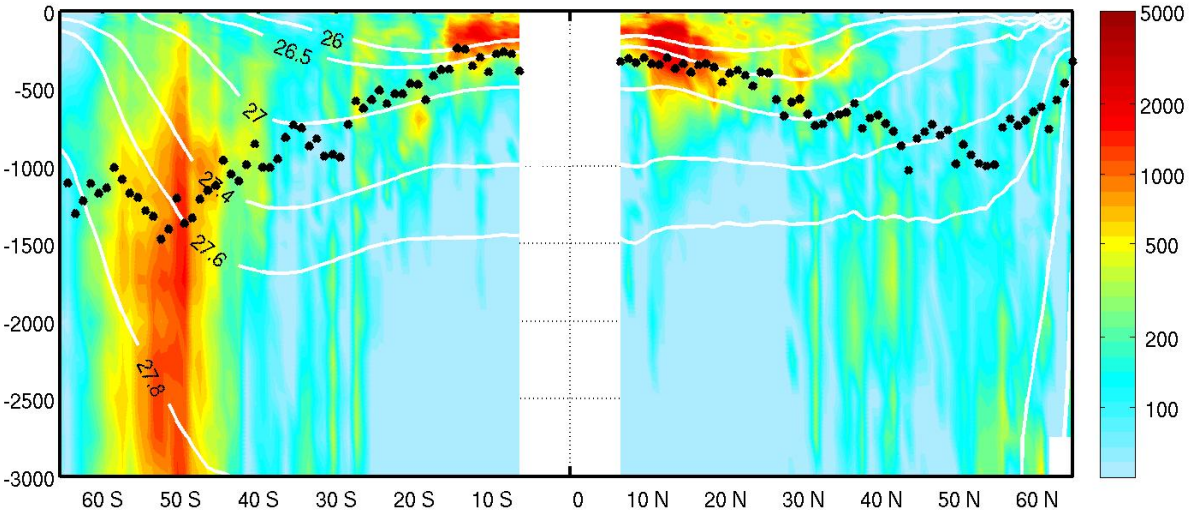


Figure 4.14.: Zonally averaged PV diffusivity $\kappa_{pv}$ [$m^2 s^{-1}$]. White lines mark the zonal mean isopycnals. Black dots mark the zonal mean steering level $|\mathbf{u}_h - \mathrm{Re}(c)| = 0$.

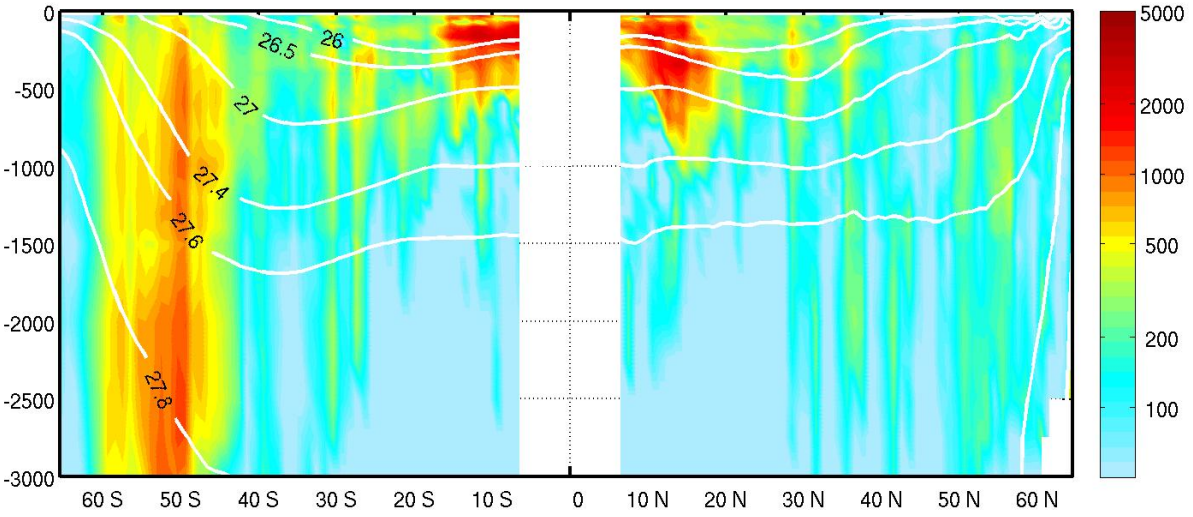


Figure 4.15.: Zonal averaged values as in fig.(4.14) but for thickness diffusivity $\kappa_b$ [$m^2 s^{-1}$]

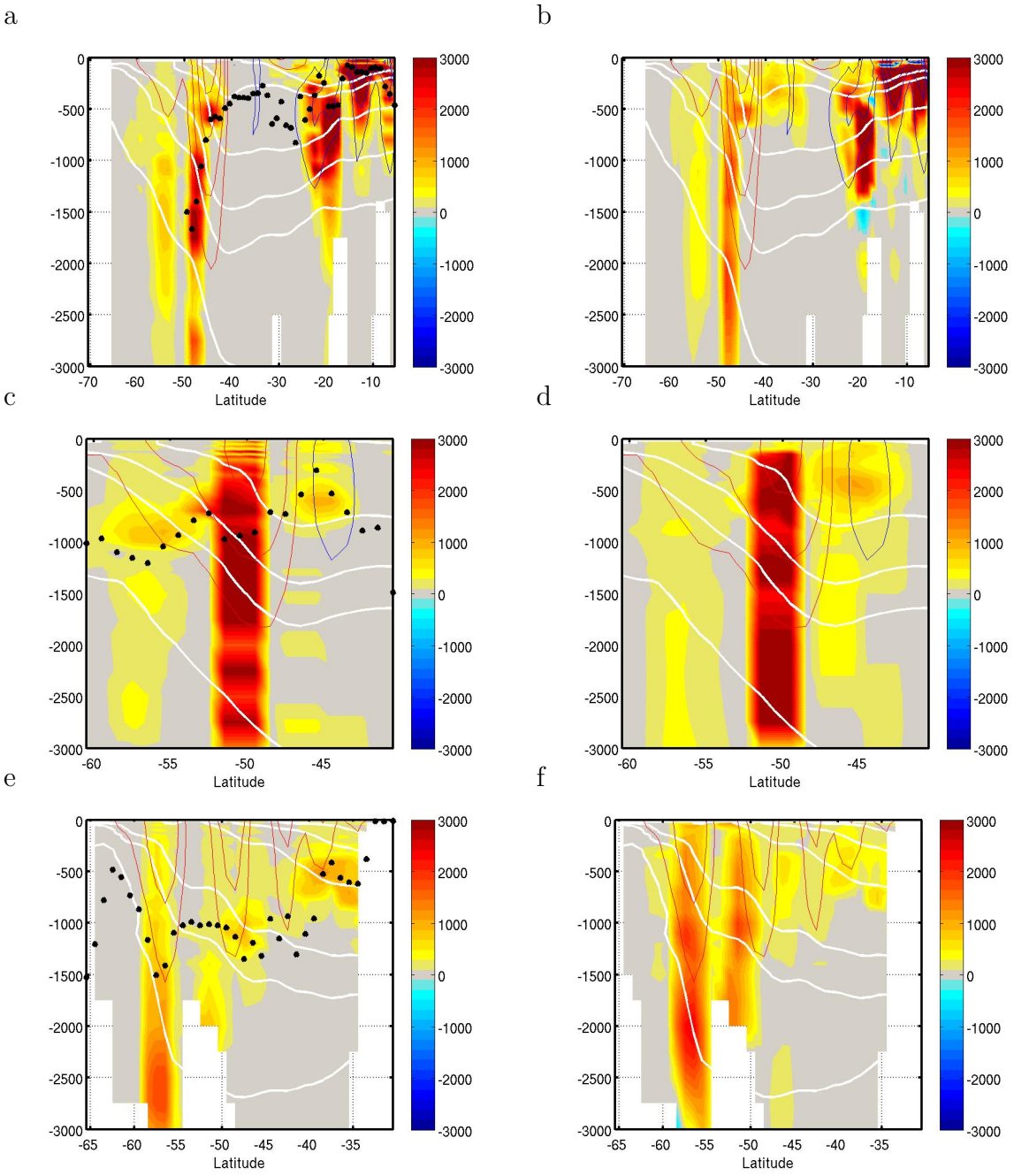


Figure 4.16.: PV diffusivity $\kappa_{pv}$ (a,c,e) and thickness-diffusivity $\kappa_b$ (b,d,f) [$m^2s^{-1}$] for chosen meridional transects in the Southern Ocean. (a,b) along 60°E. (c,d) along 130°E. (e,f) along 310°E. White lines mark isopycnals, red lines eastward zonal velocities, blue lines westward zonal velocities. Black dots mark the steering level $|\mathbf{u}_h - \mathrm{Re}(c)| = 0$.

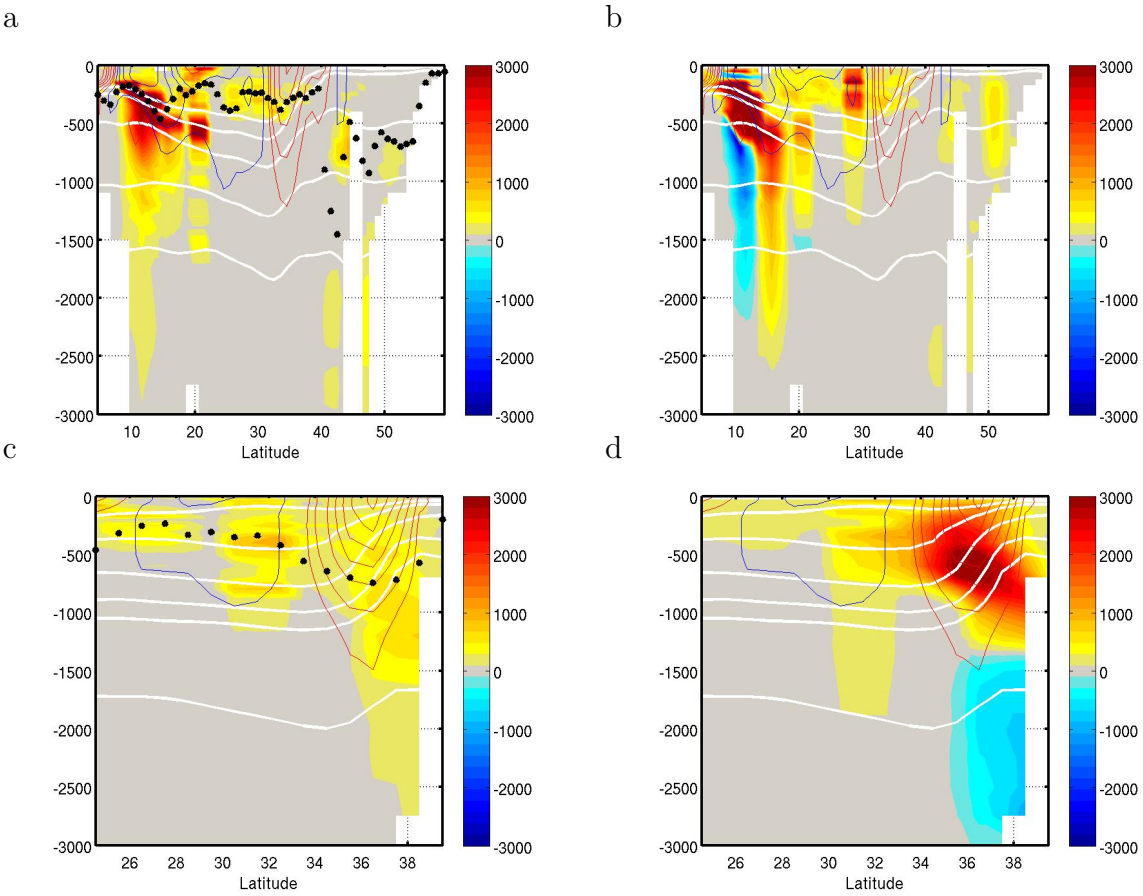


Figure 4.17.: PV diffusivity $\kappa_{pv}$ (a,c) and thickness-diffusivity $\kappa_b$ (b,d) [$m^2 s^{-1}$] for chosen meridional transects in the North Pacific and the North Atlantic. (a,b) along 150°E. (c,d) along 289°E. White lines mark isopycnals, red lines eastward zonal velocities, blue lines westward zonal velocities. Black dots mark the steering level $|\mathbf{u}_h - \mathrm{Re}(c)| = 0$.

### 4.4.3. Skewness diffusivities

Referring on the idealized profiles shown in fig.(4.4) we discussed that skewness diffusivities arise, if wavenumber vector and mean gradient of either buoyancy or potential vorticity are not perpendicular. In fig.(4.4b) the planetary vorticity gradient $\beta$ is the reason for the inclination of the wavenumber vector. In the ocean the direction of the mean potential vorticity gradient is usually varying with depth. Hence the skewness PV diffusivity $\nu_{pv}$ arises. Indeed the mean PV gradient is very noisy and changes direction frequently. In comparison to the always positive PV diffusivity $\kappa_{pv}$, the skewness PV diffusivity $\nu_{pv}$ can also obtain negative values, depending on the direction of the mean PV gradient. The dependency on the noisy mean PV gradient results in noisy skewness diffusivities $\nu_{pv}$. We skip a detailed description of the spatial dependency of $\nu_{pv}$ and focus on the spatial dependency of the skewness thickness diffusivity $\nu_b$, that indicates a clearer structure.

In comparison to the mean PV gradient the mean buoyancy gradient is smooth. As discussed in the introduction of the GM-parametrization in chapter 2.2, the skewness diffusivity $\nu_b$ represents isopycnal thickness advection. If the perturbation wave propagates diagonal to the mean buoyancy gradient, the gradient is not only reduced, but also an eddy-induced advection along or against the mean current is triggered.

Figures (4.18) and (4.19) show results for the isopycnal thickness advection $\nu_b$. Zonal mean isopycnal thickness advection $\nu_b$ is about an order of magnitude smaller than zonal mean $\kappa_b$. Fig.(4.4) shows, that it tends to be positive in eastward currents and negative in westward currents. This can be even better seen in the transects in fig.(4.19). The tendency points towards the $\beta$-effect as a main source for $\nu_b$. The currents of mixed shear in low latitudes are certainly a region, where $\nu_b$ is likely to arise as the mean buoyancy gradient changes direction with depth. Actually, in low latitudes the isopycnal thickness advection can have the same order of magnitude as downgradient thickness diffusion $\kappa_b$. The Gulf Stream transect reveals a negative $\nu_b$ in the upper 300 m and positive $\nu_b$ in the area of the main current and beneath. For a better understanding of the behavior of $\nu_b$, the dependency on the mean meridional velocity has to be studied more precisely.

A more precise investigation of the magnitude and source of $\nu_b$ exceeds the subject of this study.

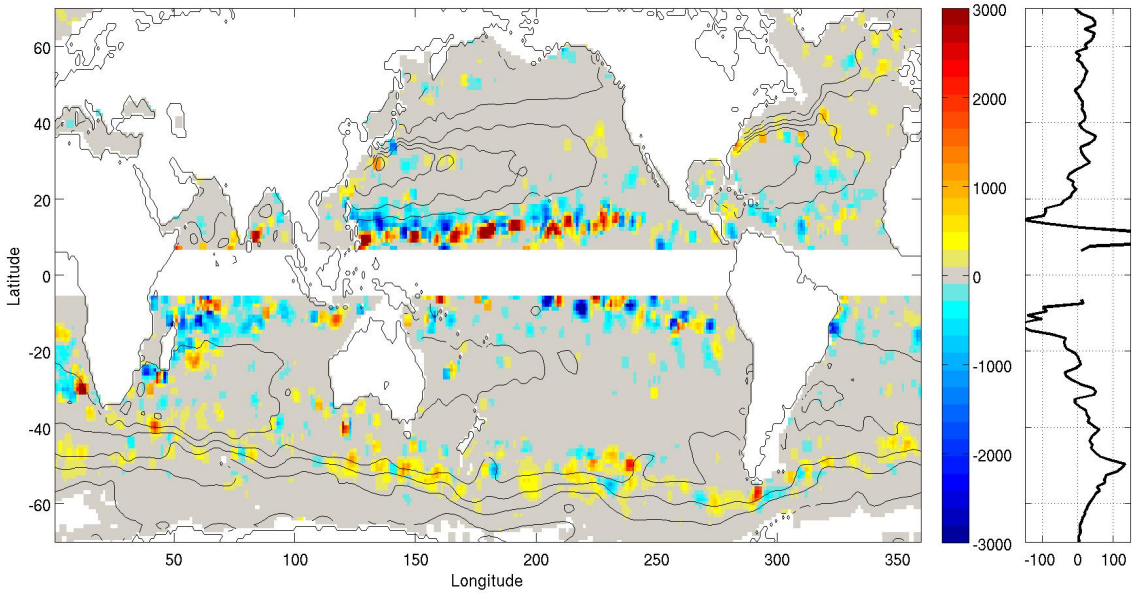


Figure 4.18.: Isopycnal thickness advection $\nu_b$ [$m^2\,s^{-1}$] in 500 m depth. The zonal average at this depth on the right hand side.

a

b

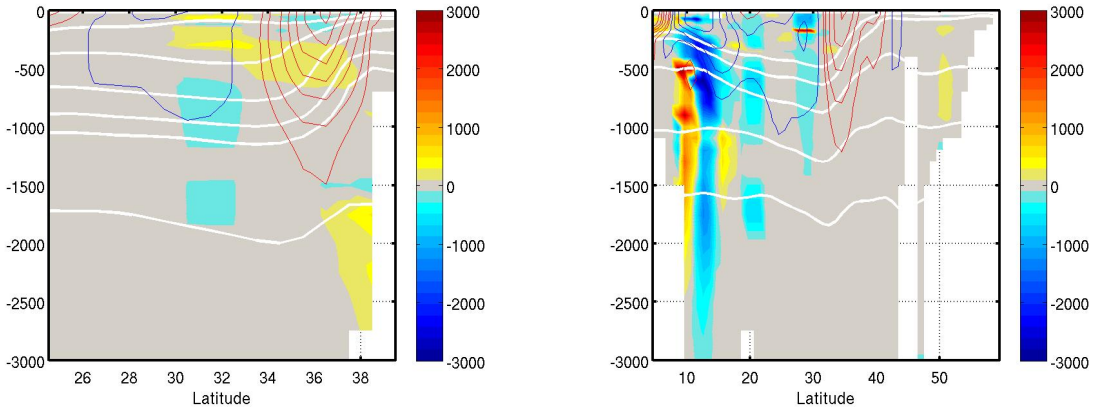


Figure 4.19.: Isopycnal thickness advection $\nu_b$ [$m^2\,s^{-1}$] for the meridional transects in (a) the North Atlantic along 289° E and (b) the North Pacific along 150° E. White lines mark isopycnals, red lines eastward zonal velocities, blue lines westward zonal velocities.

# 5. Discussion

In the following chapter we will discuss the limitations of local baroclinic linear stability analysis and make an effort to put the results of this study in respect to recent estimations of eddy time- and lengthscales and to recent diagnostics of eddy diffusivities.

## 5.1. Limitations of the local baroclinic assumption

The shown results represent a snapshot of eddy properties derived from the data of the used WOCE climatology. Methods to derive eddy diffusivities from either observations or models require a certain time span, thus the values are time-averaged values. Applying LSA on subsequent snapshots (e.g. monthly means) would certainly smooth the results to a certain degree. The structural differences, which would still exist between the shown and diagnosed eddy properties will be discussed in the following. To visualize the differences fig.(5.1) shows eddy kinetic energy (EKE) calculated from LSA compared to EKE from the eddy resolving STORM model (*von Storch et al.* (subm.)) and from satellite observations (*Scharffenberg and Stammer* (2010)). EKE can be calculated from the perturbation waves of LSA by

$$EKE = \frac{\overline{u'^2} + \overline{v'^2}}{2} = \frac{\mathrm{Re}(uu^*) + \mathrm{Re}(vv^*)}{4} = \frac{\psi_0^2}{4}(k_x^2 + k_y^2) \cdot \mathrm{Re}(\phi\phi^*) \tag{5.1}$$

Common features in the EKE images are increased values in the ACC and in the offshore regions of the GS and Kuroshio and the low EKE in the interior of the subtropical gyres. A feature also observable in all studies is the increased eddy activity in the Pacific subtropical return current. In the observations and in the model EKE is also high in the extensions of boundary currents into the open ocean, where EKE from LSA is quite low.

a

b

c

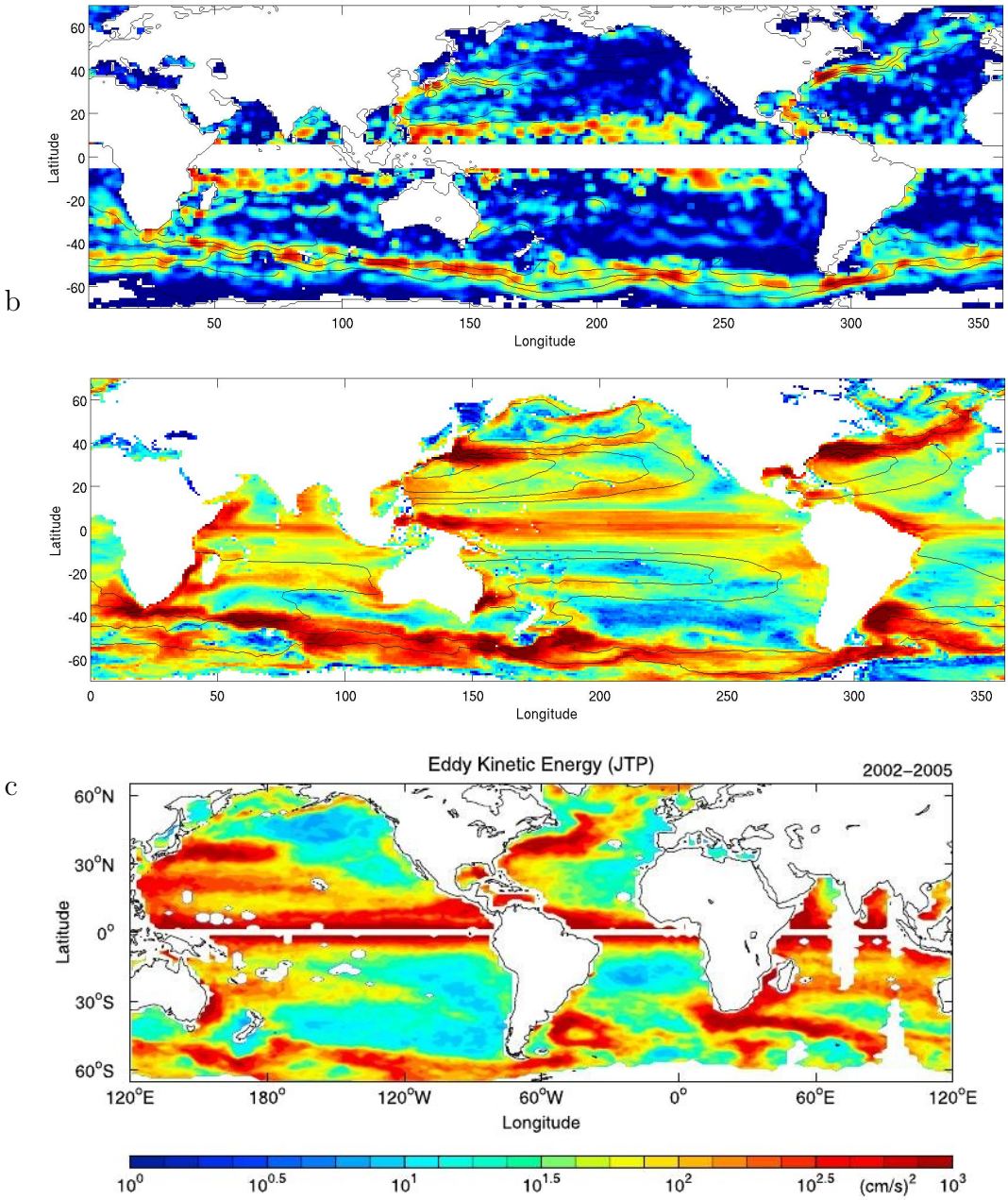


Figure 5.1.: (a) EKE [$cm^2s^2$] at 150 m depth from LSA. (b) EKE at 150 m depth from the STORM model (*von Storch et al.* (subm.)). (c) EKE from Topex-Poseidon satellite-measured sea surface height anomalies (from *Scharffenberg and Stammer* (2010)).

The difference can be linked to eddies propagating away from their source. Due to the local and linear assumptions, LSA can just identify the source of eddies, the processes that occur during the lifetime of an eddy are nonlinear turbulent processes.
Eddy kinetic energy at the equator is high in the observations, but observational errors are also high at the equator(see *Scharffenberg and Stammer* (2010)). In the STORM model, equatorial EKE is lower than EKE in the mayor currents. As noted before, linear stability analysis is not applicable near the equator as it is based on the quasi-geostrophic assumption, which is not valid for conditions at the equator. Furthermore equatorial instability waves are mostly related to barotropic shear instability processes, which are not considered in our baroclinic analysis. Shear instabilities can also play a role on the frontiers of strong currents, like south of the Gulf Stream, where horizontal shear is high.

## 5.2. Comparison with recent studies

In the following chapter we will compare the results of our study with recent studies, that use linear stability analysis to derive eddy properties and with eddy diffusivities derived by using different techniques.
*Smith* (2007) and *Tulloch et al.* (2011) use LSA to produce global maps of time- and lengthscales of meso-scale instability waves from different climatologies. The regions of high growthrates are in agreement with our results. The tendency in our results, that the lengthscale of instable waves is decoupled from the Rossby radius is also result of both studies. The lengthscale of the instable wave is larger than the Rossby radius in high latitudes and smaller in low latitudes.
When we derived the closure, we noted that the lengthscale of the fastest growing unstable wave is not equal to the final eddy lengthscale. Nonlinear processes influence the final eddy lengthscale and it is usually larger than the lengthscale of the fastest growing mode. However, different observational studies support the assumption, that the eddy scale varies less with latitude than the Rossby radius (e.g. *Chelton et al.* (2007), *Eden*

a b

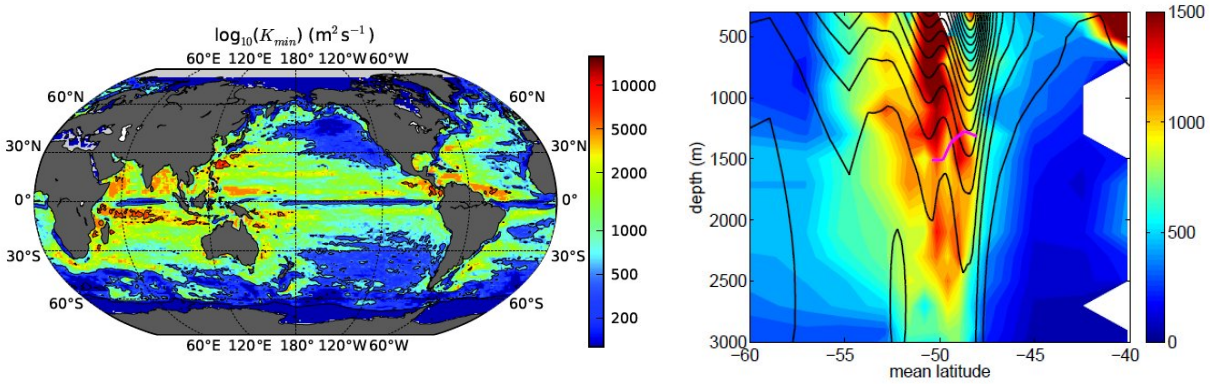


Figure 5.2.: Different estimates of meso-scale eddy diffusivities of passive tracers. (a) Effective Osborn-Cox Diffusivity of a passive tracer derived from a 1/3° ocean surface model. From Abernathey et al. (submitted). (b) Isopycnal (cross mean temperature contours) Lagrangian diffusivity [$m^2s^{-1}$] in the Southern Ocean averaged between 120° E and 160° E derived from a 1/10° model. From Griesel et al. (submitted)

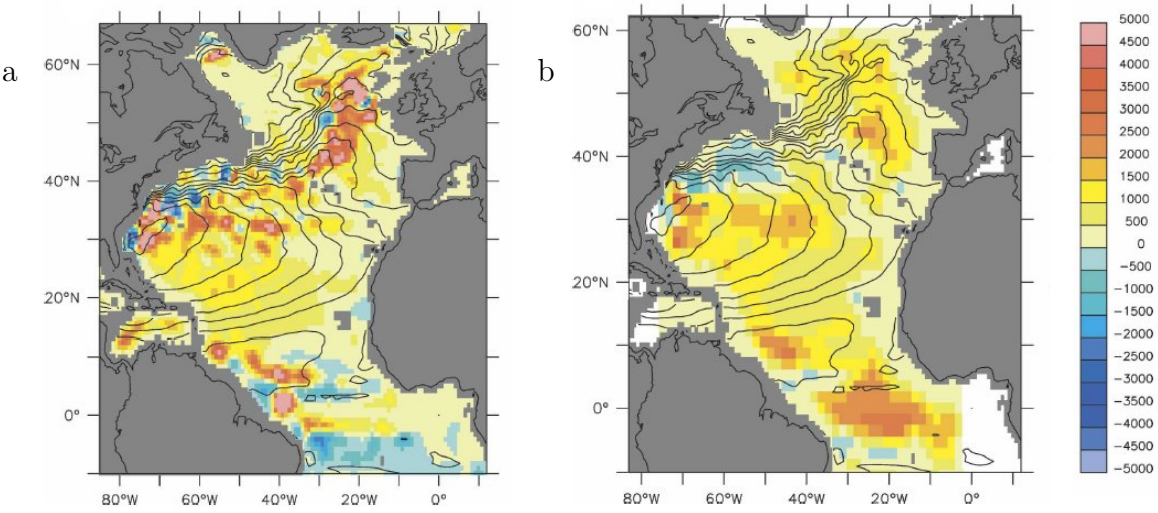


Figure 5.3.: Different estimates of thickness diffusivity $\kappa_b$ [$m^2s^{-1}$] in 300 m depth from eddy fluxes from which different rotational fluxes have been removed. Eddy fluxes are calculated from a 1/12° eddy-resolving model. From *Eden et al.* (2007)

(2007)). The approximate lengthscale $L_{bc}$ used in this study is based on the study by *Eden* (2007). *Eden* (2007) analyzes eddy lengthscales derived from satellite observations and model simulations and finds scales proportional to the Rossby radius in high latitudes and scales proportional to the Rhine's scale in low latitudes.

The effect of a topographic slope on the magnitude of a vertically constant thickness diffusivity is subject of a study by *Isachsen* (2011). *Isachsen* (2011) compares LSA results with an idealized model in high latitudes. The tendency for diffusivities to decrease for topographic slopes is a result of the idealized model. The maximum of diffusivities, that result from LSA, for a slight orthogonal slope is not found in the model simulation. Thus it is stated, that linear stability theory is only partly able to represent the influence of topography on eddy properties.

Multiple methods exist to diagnose meso-scale eddy diffusivities from eddy-resolving models, adjoined models or satellite observations. Most studies calculate passive tracer diffusivities, which can be rather compared to PV diffusivity than to thickness diffusivity as argued by *Nakamura* (1996) and *Smith and Marshall* (2009). The increased PV diffusivities at mid-depth in the Southern Ocean are in line with current studies of *Smith and Marshall* (2009) and *Abernathey et al.* (2010). *Smith and Marshall* (2009) also uses linear stability analysis and compares the result with a simple nonlinear model. Both results support the mid-depth mixing theory in the ACC.

*Abernathey et al.* (2010) is showing effective Osborn-Cox diffusivity derived from an eddy-permitting Southern Ocean model. Effective diffusivity represents Lagrangian passive tracer mixing, Effective diffusivity is increased at mid-depth in the ACC, but increased mixing rates are also found near the surface in the equatorward flank of the ACC. The later feature is not present in our study. *Abernathey et al.* (2010) claim that it is most likely related to the propagation of strong Agulhas eddies and eddies downstream of Drake passage.

In a recent submitted study by Abernathey, satellite sea-surface height anomalies are used to drive a surface model and calculate surface effective diffusivity. The global map shown in fig.5.2a is characterised by high diffusivities in the westward currents in the

Pacific and Indian Oceans and the offshore regions of the boundary Pacific and Atlantic boundary currents. Diffusivities in the ACC are low with the exception of the current systems around South Africa. The zonal average of effective surface diffusivity looks very similar to the zonal mean PV diffusivity from LSA in 150 m depth shown in fig.(4.12a). *Griesel et al.* (subm.) calculate the dispersion of floats in an eddy-resolving model to derive Lagrangian cross-stream diffusivities in the Southern Ocean. The dominant regions of high diffusivity are near the surface equatorwards of the ACC, like in *Abernathey et al.* (2010). But in regions, where the ACC is characterised by one dominant jet as shown in fig.(5.2b), they find structures similar to the transects from LSA shown in fig.(4.16).

The comparison of PV diffusivity from LSA with diagnosed passive tracer diffusivities shows, that the mentioned nonlinear factors, that are not present in linear stability analysis, can have a large influence on eddy diffusivities in the vicinity of strong currents. The main factor seems to be the radiation of eddies into weakly sheared areas. However, most notably the studies by *Griesel et al.* (subm.) and *Smith and Marshall* (2009) indicate, that LSA is able to describe the structure of eddy diffusivity inside strong current regimes.

Studies of thickness diffusivity based on high resolution models suffer from the fact, that they have to account for a rotational flux, which is created by rotating eddies and needs to be removed to detect the effect eddies have on the mean density field.

*Eden et al.* (2007) and *Eden* (2006) show thickness diffusivities $\kappa_b$ and isopycnal thickness advection $\nu_b$ in the North Atlantic and Southern Ocean respectively. In the ACC they get a structure of thickness diffusivity rather similar to the PV diffusivity shown in this study, with a dominant interior maximum at the steering level. In the upper Gulf Stream they actually calculate negative thickness diffusivities even after removing different rotational fluxes (see fig.(5.3)). Thickness diffusivity is higher and positive south of the GS. Isopycnal thickness advection $\nu_b$ is positive in the GS and negative in the ACC. The result in the GS matches with our results, but diffusivities from LSA are positive in the ACC as well.

Studies by *Ferreira et al.* (2005) and *Liu et al.* (2012) also support the finding, that thickness diffusivity can obtain negative values in strong current systems.
*Eden* (2011) is supporting the depth-intensified structure of thickness diffusivities in the ACC in an simplified eddy-resolving model study with flat bottom. The differences between thickness diffusivity from LSA and diagnosed thickness diffusivity are more complex than the differences between PV- and tracer diffusivity. The diagnosis of thickness diffusivity seems to be highly related to the used model and method.
Idealized models like the one used in *Eden* (2011) indicate that thickness diffusivities from LSA are able to reproduce thickness diffusivities from eddy-resolving models.

# 6. Summary and Outlook

The magnitude and spatial dependency of meso-scale eddy diffusivities plays an important role for parametrizations of meso-scale fluxes in low resolution ocean models. Considering the complexity of ocean background conditions, it is difficult to distinguish the factors, that influence magnitude and spatial dependency of eddy diffusivities in the ocean. Using a closure based on a numeric solution of the local linear stability problem, we started with the simplest case, the *Eady* (1949) background conditions and added planetary vorticity, topographic slopes, and depth-dependent potential vorticity subsequently.

Eady conditions are a constant vertical velocity shear, a constant stratification and no planetary vorticity gradient. For these conditions thickness diffusivity is vertically constant and PV diffusivity is symmetric to the steering level at mid-depth. Eady's analytic solution links the lengthscale to the first baroclinic Rossby radius and the growthrate to the local Richardson number.

We show that Eady's analytic solution breaks down in combination with large relations of $\beta/\nabla\overline{q}$ and $\nabla h^*/\nabla\overline{q}$. In other words, time- and lenghtscales of the solution are modified, if the vorticity gradient created by either planetary vorticity or the topographic slope has the same order as the gradient created by vertical shear of velocities. These insights can be carried over to the solution for the more complex profiles from climatological data.

Lengthscales of the instable waves in low latitudes are smaller than predicted by Eady. The absolute lengthscale remains quite constant polewards of 20 degrees. The stability due to topographic slopes is large in the subpolar ocean polewards of 40 degrees, with

reductions of growthrates and lengthscales of around 20 percent. These less instable and smaller perturbation waves lead to significant smaller diffusivities especially in the ACC.

The vertical structure of diffusivities in constantly sheared profiles depends on the angle to the planetary vorticity gradient $\beta$. Eastward currents have a depth-increasing structure of diffusivities, westward currents a depth-decaying structure. PV diffusivity differs from thickness diffusivity mainly by the local increase at the steering level. A consequence of the steering level is that the global distribution of thickness diffusivity is smoother than the global distribution of PV diffusivity.

Idealized profiles with a more realistic surface-intensified shear reveal that westward currents are more unstable and produce higher eddy diffusivities than eastward currents. A consequence is that high diffusivities result in the westward return currents between 10° - 20° north and south of the equator. In comparison, diffusivities in surface intensified eastward currents like the GS and the Kuroshio are low . Diffusivities of the deep ACC are high and increase towards depth, which is an indication, that the ACC can be well approximated with Eady conditions.

We discussed the limits of linear stability analysis which are consequences of the neglect of nonlinear effects and of the local baroclinic assumption. We show that our results are similar to diagnosed eddy diffusivities from eddy-resolving models or observations, considering the limits of LSA. The main aspects, that are consistent with other studies are the following.

We find high near surface eddy diffusivities in low latitudes related to westward mean flow. Furthermore we find an increased PV diffusivity at the steering level along with suppression at the surface and a suppression of diffusivities by topographic slopes in high latitudes.

It is difficult to assume the impact of the calculated meso-scale eddy diffusivities on the ocean circulation in a model parametrization. The circulation-pattern would react on the magnitude of the diffusivities and the net impact has to be evaluated. A problem would certainly arise from the noisiness of the results related to the switch between

different growing modes. Another problem would be the high computational effort. We show that a simple approximation of the amplitude of diffusivities by using the local Richardson number would lead to an overestimation of diffusivities in high latitudes and an underestimation in low latitudes. This effect can be mainly linked to the influences of topography and planetary $\beta$.

An attempt to reduce the computational effort of LSA is made in *Killworth* (1997) and in *Eden* (2012, in press) by constructing an approximate solution of linear stability analysis in form of a power series. The effect of eddy propagation away from their origin is addressed in *Eden and Greatbatch* (2008) by implementing a radiation scheme of eddy kinetic energy, that would complement the results from linear stability analysis. An approach to increase the information delivered by linear stability analysis is to increase the complexity by including ageostrophic motion and horizontal shear. The inclusion of ageostrophic motion allows to extend the analysis on the oceanic mixed layer. An inclusion of horizontal shear would allow to study the magnitude of barotropic instability.

# Bibliography


Abernathey, R., J. Marshall, M. Mazloff, and E. Shuckburgh (2010), Enhancement of mesoscale eddy stirring at steering levels in the southern ocean, *Journal of Physical Oceanography*, *40*(1), 170–184.

Bauer, S., M. Swenson, and A. Griffa (2002), Eddy mean flow decomposition and eddy diffusivity estimates in the tropical pacific ocean: 2. results, *Journal of Geophysical Research*, *107*(C10), 3154.

Beckmann, A. (1988), Vertical structure of midlatitude mesoscale instabilities, *Journal of physical oceanography*, *18*(10), 1354–1371.

Charney, J. (1947), The dynamics of long waves in a baroclinic westerly current, *J. Meteor*, *4*(5), 135–161.

Chelton, D., M. Schlax, R. Samelson, and R. de Szoeke (2007), Global observations of large oceanic eddies, *Geophysical Research Letters*, *34*(15), L15,606.

Eady, E. (1949), Long waves and cyclone waves, *Tellus*, *1*(3), 33–52.

Eden, C. (2006), Thickness diffusivity in the antarctic circumpolar current, *Geophys. Res. Letters*, *33*, 354.

Eden, C. (2007), Eddy length scales in the north atlantic ocean, *Journal of geophysical research*, *112*(C6), C06,004.

Eden, C. (2010), Parameterising meso-scale eddy momentum fluxes based on potential vorticity mixing and a gauge term, *Ocean Modelling*, *32*(1-2), 58–71.

Eden, C. (2011), A closure for meso-scale eddy fluxes based on linear instability theory, *Ocean Modelling*, *39*, 362–369.

Eden, C., and R. Greatbatch (2008), Towards a mesoscale eddy closure, *Ocean Modelling*, *20*(3), 223–239.

Eden, C., R. Greatbatch, and J. Willebrand (2007), A diagnosis of thickness fluxes in an eddy-resolving model, *Journal of physical oceanography*, *37*(3), 727–742.

Eden, C., M. Jochum, and G. Danabasoglu (2009), Effects of different closures for thickness diffusivity, *Ocean Modelling*, *26*(1-2), 47–59.

Ferreira, D., J. Marshall, and P. Heimbach (2005), Estimating eddy stresses by fitting dynamics to observations using a residual-mean ocean circulation model and its adjoint, *Journal of Physical Oceanography*, *35*(10), 1891–1910.

Gent, P., and J. McWilliams (1990), Isopycnal mixing in ocean circulation models, *J. Phys. Oceanogr*, *20*(1), 150–155.

Gill, A., J. Green, and A. Simmons (1974), Energy partition in the large-scale ocean circulation and the production of mid-ocean eddies, in *Deep Sea Research and Oceanographic Abstracts*, vol. 21, pp. 499–508, Elsevier.

Gouretski, V., and K. Koltermann (2004), Woce global hydrographic climatology, *Berichte des BSH*, *35*, 1–52.

Green, J. (1970), Transfer properties of the large-scale eddies and the general circulation of the atmosphere, *Quarterly Journal of the Royal Meteorological Society*, *96*(408), 157–185.

Hristova, H., J. Pedlosky, and M. Spall (2010), Radiating instability of a meridional boundary current.

Isachsen, P. (2011), Baroclinic instability and eddy tracer transport across sloping bottom topography: How well does a modified eady model do in primitive equation simulations?, *Ocean Modelling*, *39*(1), 183–199.

Killworth, P. (1997), On the parameterization of eddy transfer part i. theory, *Journal of marine research*, *55*(6), 1171–1197.

Liu, C., A. Köhl, and D. Stammer (2012), Adjoint based estimation of eddy induced tracer mixing parameters in the global ocean, *Journal of Physical Oceanography*, (2012).

Marshall, J. (1981), On the parameterization of geostrophic eddies in the ocean, *Journal of Physical Oceanography*, *11*, 257–271.

Marshall, J., E. Shuckburgh, H. Jones, and C. Hill (2006), Estimates and implications of surface eddy diffusivity in the southern ocean derived from tracer transport, *Journal of physical oceanography*, *36*(9), 1806–1821.

Nakamura, N. (1996), Two-dimensional mixing, edge formation, and permeability diagnosed in an area coordinate, *Journal of the atmospheric sciences*, *53*(11), 1524–1537.

Olbers, D., J. Willebrand, and C. Eden (2012), Ocean dynamics.

Phillips, N. (1954), Energy transformations and meridional circulations associated with simple baroclinic waves in a two-level, quasi-geostrophic model1, *Tellus*, *6*(3), 273–286.

Robinson, A., and J. McWilliams (1974), The baroclinic instability of the open ocean, *Journal of Physical Oceanography*, *4*, 281–294.

Scharffenberg, M., and D. Stammer (2010), Seasonal variations of the large-scale geostrophic flow field and eddy kinetic energy inferred from the topex/poseidon and jason-1 tandem mission data, *Journal of Geophysical Research*, *115*(C2), C02,008.

Smith, K. (2007), The geography of linear baroclinic instability in earth's oceans, *Journal of Marine Research*, *65*(5), 655–683.

Smith, K., and J. Marshall (2009), Evidence for enhanced eddy mixing at middepth in the southern ocean, *Journal of Physical Oceanography*, *39*(1), 50–69.

Stammer, D. (1998), On eddy characteristics, eddy transports, and mean flow properties, *Journal of Physical Oceanography*, *28*(4), 727–739.

Tulloch, R., J. Marshall, C. Hill, and K. Smith (2011), Scales, growth rates and spectral fluxes of baroclinic instability in the ocean, *Journal of Physical Oceanography*.

Visbeck, M., J. Marshall, T. Haine, and M. Spall (1997), Specification of eddy transfer coefficients in coarse-resolution ocean circulation models*, *Journal of Physical Oceanography*, *27*(3), 381–402.

von Storch, J., C. Eden, I. Fast, H. Haak, D. Hernandez-Deckers, E. Maier-Reimer, J. Marotzke, and D. Stammer (subm.), An estimate of the lorenz energy cycle for the world ocean based on the 1/10 storm/ncep simulation, *Journal of Physical Oceanography*.

# A. Appendix

## A.1. Modification of LSA for use with climatological data

Using linear stability analysis with profiles from climatological or model data creates several problems. In this section the dominant issues will be addressed and the applied methods are presented:

**Numerical noise and small scale perturbations** The process of baroclinic instability is closely linked to the mean PV gradient. As the PV gradient is usually not a variable used in models and is not taken into account in the construction of climatologies, it has to be calculated with a finite difference method using the model grid, stratification and velocities. This calculation introduces noise in the gradient, which in this case usually leads to multiple zero-crossings in the vertical profile due to small changes in the vertical derivative of the velocities. The waves excited by these zero-crossings are closely related to the few grid points in which the crossings occur and tend to dominate the solution for small wavelengths. As we are mainly interested in the modes relevant for meso-scale mixing, which are in the range of the first baroclinic Rossby Radius, these small scale perturbations need to be suppressed or filtered to receive the baroclinic modes. In our script we address this issue by introducing a horizontal isotropic friction parameter $A_h$ in the potential vorticity equation (2.17).

$$\partial_t q' + \overline{\mathbf{u}_h} \cdot \nabla q' + \mathbf{u}' \cdot \nabla \overline{q} = A_h \nabla^2 q' \tag{A.1}$$

In so doing higher wavenumbers are damped relative to the value of $A_h$. We chose $A_h = 10\mathrm{m}^2\mathrm{s}^{-1}$ as it is often used in ocean models and as it seems to represent a reasonable compromise between preserving the growthrates of the desired modes and damping the small scale modes.

**Mixed Layer** The Ocean mixed layer is characterized by a very low stratification N. As the PV gradient is proportional to $N^{-2}$, small velocity-shear variations create very large PV gradients. The corresponding mixed layer instabilities have high growthrates and dominate the wavenumber space at high wavenumbers. As we are interested in the interior baroclinic modes and as the growthrates of mixed layer instabilities can only be suppressed by large friction $A_h$, which also effects the baroclinic modes, the mixed layer is excluded from the analysis. This is implemented by introducing a threshold for the difference of density at the surface and in the regarded layer, which has to be exceeded for the data to be included in the analysis. The threshold chosen is $\Delta\rho = 0.015 kgm^{-3}$.

**Direction of propagation** The distribution of growthrates in wavenumber space is symmetric. Which means that the solution delivers two possible directions of wave propagationfor the fastest growing wave, which are valid. The direction has a mayor influence on meso-scale mixing as upgradient mixing would occur, if the wave propagates upstream, and downgradient mixing, if the wave propagates downstream in a geostrophically balanced flow. A way to construct a measure for the direction of wave propagation is to assume that the vertical integral of thickness diffusion is downgradient (as considered in the GM parametrization). So while it is possible that negative thickness diffusivities exist, the perception is, that in the vertical mean the effect of meso-scale eddies is a release of potential energy. So for a pair of wavenumbers $k_x$ and $k_y$, the condition is that

$$\int_{-h}^{0} \kappa_b(k_x, k_y)\, dz > 0. \tag{A.2}$$

## A.2. Discretization of the linear stability problem

**The discrete stretching operator** Following *Smith* (2007), the discrete stretching operator $\Gamma_{nm}$ is

$$\Gamma_{nm}\Psi_m = \frac{f^2\rho_0}{g}\begin{cases} \frac{1}{\delta_1}\left(\frac{\Psi_2-\Psi_1}{\rho_2-\rho_1}\right), & n=1 \\ \frac{1}{\delta_n}\left(\frac{\Psi_{n-1}-\Psi_n}{\rho_n-\rho_{n-1}} - \frac{\Psi_n-\Psi_{n+1}}{\rho_{n+1}-\rho_n}\right), & n=2...N-1 \\ \frac{1}{\delta_N}\left(\frac{\Psi_{N-1}-\Psi_N}{\rho_N-\rho_{N-1}}\right), & n=N \end{cases} \tag{A.3}$$

,where $\delta_n = (\Delta_{n-1} + \Delta_n)/2$ and $\Delta_n$ the spacing between the $\Psi_n$ and $\Psi_{n+1}$.

**The discrete PV-gradient** The discrete PV-gradient is computed using the discrete stretching operator:

$$\nabla\overline{q}_n = \Gamma_{nm}\overline{v}_m\hat{\mathbf{i}} + (\beta - \Gamma_{nm}\overline{u}_m)\,\hat{\mathbf{j}} \tag{A.4}$$

In presence of a topographic slopes $h_x$ and $h_y$ the bottom level is modified to:

$$\nabla\overline{q}_N = \left(\frac{fh_x}{\Delta_N} + \Gamma_{Nm}\overline{v}_m\right)\hat{\mathbf{i}} + \left(\frac{fh_y}{\Delta_N} + \beta - \Gamma_{Nm}\overline{u}_m\right)\hat{\mathbf{j}}. \tag{A.5}$$

The slopes are calculated from the topography of the WOCE climatology. The $0.5x0.5$ data is smoothed with a $2x2$ running mean to remove small scale disturbance.

**Discretization** Without a background current the discrete version of eq.(2.19) is

$$B_{ij}\phi_j = 0$$

,with $B_{ij} = \Gamma_{ij} - k^2\delta_{ij}$. The $\delta$s are Kronecker deltas, which equal unity if the indices are equal and zero otherwise. The problem without background velocities delivers eigenvalues k and vertical eigenmodes of the stable wave responses, the Rossby waves. The smallest eigenvalue k corresponds to the barotropic mode and the second smallest k

corresponds to the first baroclinic Rossby-radius $L_{Ro} = k_2^{-1}$, which is compared with the scales of the unstable waves. The full problem may be written:

$$\omega B_{ij}\phi_j = A_{ij}\phi_j$$

where

$$A_{ij} = k\tilde{\beta}^m \delta_{ijm} + k\tilde{U}^m \delta_{inm} B_{nj}.$$

When friction is included $A_{ij}$ becomes

$$A_{ij} = k\tilde{\beta}^m \delta_{ijm} + k\tilde{U}^m \delta_{inm} B_{nj} - \sqrt{-1} A_h k^2 \delta_{ij} B_{ij}.$$

The boundary conditions are included by the discrete stretching operator. For N depth levels, the solution consists of N eigenvectors $\phi$ and eigenvalues $\omega$.

# B. Danksagung

Diese Arbeit entstand in der Abteilung der theoretischen Ozeanographie am Institut für Meereskunde in Hamburg. Ich möchte mich bei Prof. Carsten Eden für die Betreuung der Masterarbeit bedanken.
Vielen Dank an Hannah Kleppin und David Bröhan für das Korrekturlesen und für Verbesserungsvorschläge.
Ich danke meinen Dozenten und Kommilitonen für ein lehrreiches und angenehmes Studium.

# C. Erklärung

Hiermit erkläre ich, dass ich die vorliegende Masterarbeit selbstständig verfasst und keine anderen als die angegebenen Quellen und Hilfsmittel verwendet habe. Desweiteren versichere ich, dass ich die Abschlussarbeit nicht bereits in einem anderen Prüfungsverfahren eingereicht habe. Ich erkläre mich damit einverstanden, dass ein Exemplar der Abschlussarbeit der Institutsbibliothek zur Verfügung gestellt wird. Die eingereichte schriftliche Fassung und die Fassung auf dem eingereichten Speichermedium sind identisch.

Hamburg, den 4.1.2013